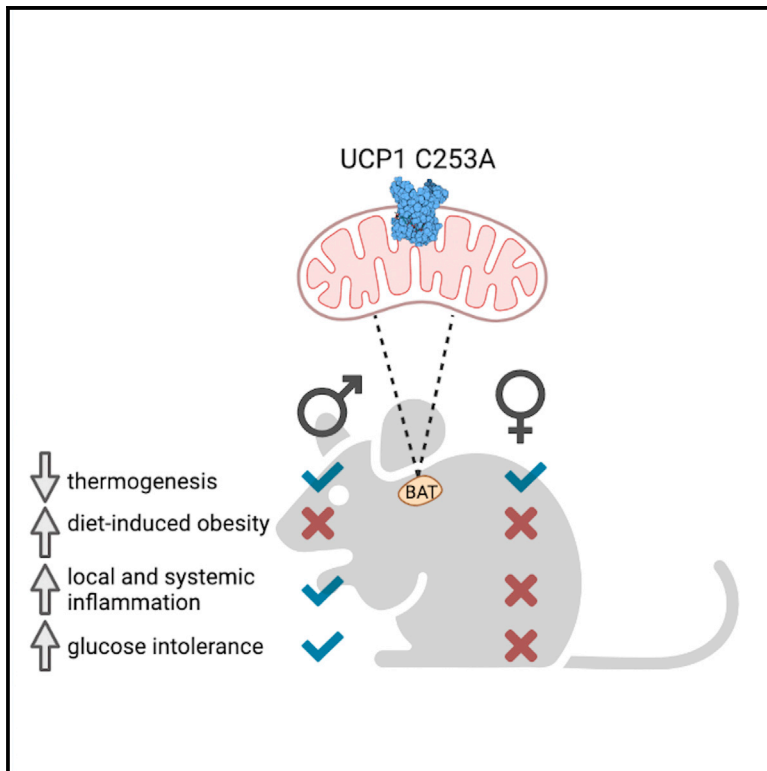# Cysteine 253 of UCP1 regulates energy expenditure and sex-dependent adipose tissue inflammation

Graphical abstract

Authors

Evanna L. Mills, Cathal Harmon, Mark P. Jedrychowski, ..., Steven P. Gygi, Bruce M. Spiegelman, Edward T. Chouchani

Correspondence

edwardt_chouchani@dfci.harvard.edu

In brief

Mills et al. examine the physiological importance of cysteine-253 in uncoupling protein 1 (UCP1), a major regulator of adipocyte thermogenesis. They find that mice lacking UCP1 C253 exhibit significantly compromised thermogenic responses and an unexpected elevation in adipose tissue redox stress, which drives substantial immune cell infiltration and systemic inflammatory pathology in adipose tissues and livers of male, but not female, mice.

Highlights

- UCP1 C253A is a precise genetic model for selective disruption of UCP1 *in vivo*

- Mutation of UCP1 C253 compromises thermogenesis but has no effect on diet-induced obesity

- UCP1 C253 regulates inflammation and glucose tolerance in male mice

- Elevation of systemic estrogen reverses male-specific pathology in UCP1 C253A mice

Article

Cysteine 253 of UCP1 regulates energy expenditure and sex-dependent adipose tissue inflammation

Evanna L. Mills,[1,2] Cathal Harmon,[4,5] Mark P. Jedrychowski,[1,2] Haopeng Xiao,[1,2] Anja V. Gruszczyk,[7] Gary A. Bradshaw,[3] Nhien Tran,[1] Ryan Garrity,[1] Dina Laznik-Bogoslavski,[1] John Szpyt,[2] Hannah Prendeville,[6] Lydia Lynch,[4,5,6] Michael P. Murphy,[7,8] Steven P. Gygi,[2] Bruce M. Spiegelman,[1,2] and Edward T. Chouchani[1,2,9,*]
[1]Department of Cancer Biology, Dana-Farber Cancer Institute, Boston, MA, USA
[2]Department of Cell Biology, Harvard Medical School, Boston, MA, USA
[3]Harvard Program in Therapeutic Science, Harvard Medical School, Boston, MA, USA
[4]Department of Immunology, Harvard Medical School, Boston, MA, USA
[5]Division of Endocrinology, Diabetes and Hypertension, Brigham and Women's Hospital and Harvard Medical School, Boston, USA
[6]School of Biochemistry and Immunology, Trinity College Dublin, Dublin, Ireland
[7]Medical Research Council Mitochondrial Biology Unit, University of Cambridge, Cambridge CB2 0XY, UK
[8]Department of Medicine, University of Cambridge, Cambridge CB2 0QQ, UK
[9]Lead contact
*Correspondence: edwardt_chouchani@dfci.harvard.edu
https://doi.org/10.1016/j.cmet.2021.11.003

SUMMARY

Uncoupling protein 1 (UCP1) is a major regulator of brown and beige adipocyte energy expenditure and metabolic homeostasis. However, the widely employed UCP1 loss-of-function model has recently been shown to have a severe deficiency in the entire electron transport chain of thermogenic fat. As such, the role of UCP1 in metabolic regulation *in vivo* remains unclear. We recently identified cysteine-253 as a regulatory site on UCP1 that elevates protein activity upon covalent modification. Here, we examine the physiological importance of this site through the generation of a UCP1 cysteine-253-null (UCP1 C253A) mouse, a precise genetic model for selective disruption of UCP1 *in vivo*. UCP1 C253A mice exhibit significantly compromised thermogenic responses in both males and females but display no measurable effect on fat accumulation in an obesogenic environment. Unexpectedly, we find that a lack of C253 results in adipose tissue redox stress, which drives substantial immune cell infiltration and systemic inflammatory pathology in adipose tissues and liver of male, but not female, mice. Elevation of systemic estrogen reverses this male-specific pathology, providing a basis for protection from inflammation due to loss of UCP1 C253 in females. Together, our results establish the UCP1 C253 activation site as a regulator of acute thermogenesis and sex-dependent tissue inflammation.

INTRODUCTION

The extraordinary capacity for thermogenic adipocytes to oxidize fuels in futile cycles to counteract obesity has generated considerable interest in understanding the mechanisms that control these processes. This interest has been further stimulated by findings demonstrating substantial quantities of brown and beige fat in adult humans (Becher et al., 2021; Cypess et al., 2009; van Marken Lichtenbelt et al., 2009; Virtanen et al., 2009). Seminal studies have now identified distinct lineages of thermogenic-competent adipocytes and the molecular factors that control their identity and differentiation (reviewed in Shapira and Seale, 2019). A question of similar importance from a therapeutic standpoint is how thermogenic respiration is activated in these cells (Chouchani et al., 2019). This question is particularly relevant since brown adipose tissue (BAT) is predominantly quiescent under basal conditions and requires activation by pe-

ripheral signals for thermogenic respiration to occur (Cannon and Nedergaard, 2004; Muzik et al., 2017).

In both rodents and humans, the best-characterized interventions that drive BAT thermogenesis are cold exposure and β-adrenoreceptor agonism. These stimuli result in clearance of glucose and fatty acids from the blood by BAT, increased energy expenditure, and protection against insulin resistance (Baskin et al., 2018; Bordicchia et al., 2012; Chen et al., 2013b; Cypess et al., 2015; Lafontan and Berlan, 1993; Liu et al., 2016; Orava et al., 2011; Ouellet et al., 2012). The above interventions initiate adipose tissue thermogenesis in part by activating the thermogenic effector uncoupling protein 1 (UCP1), a protein uniquely expressed in BAT and beige fat. Importantly, UCP1 remains inactive under basal conditions, but when activated, it initiates proton leak across the mitochondrial inner membrane, which is sufficient to substantially elevate catabolism of reduced substrates derived from glucose and fats (Chouchani et al., 2019).
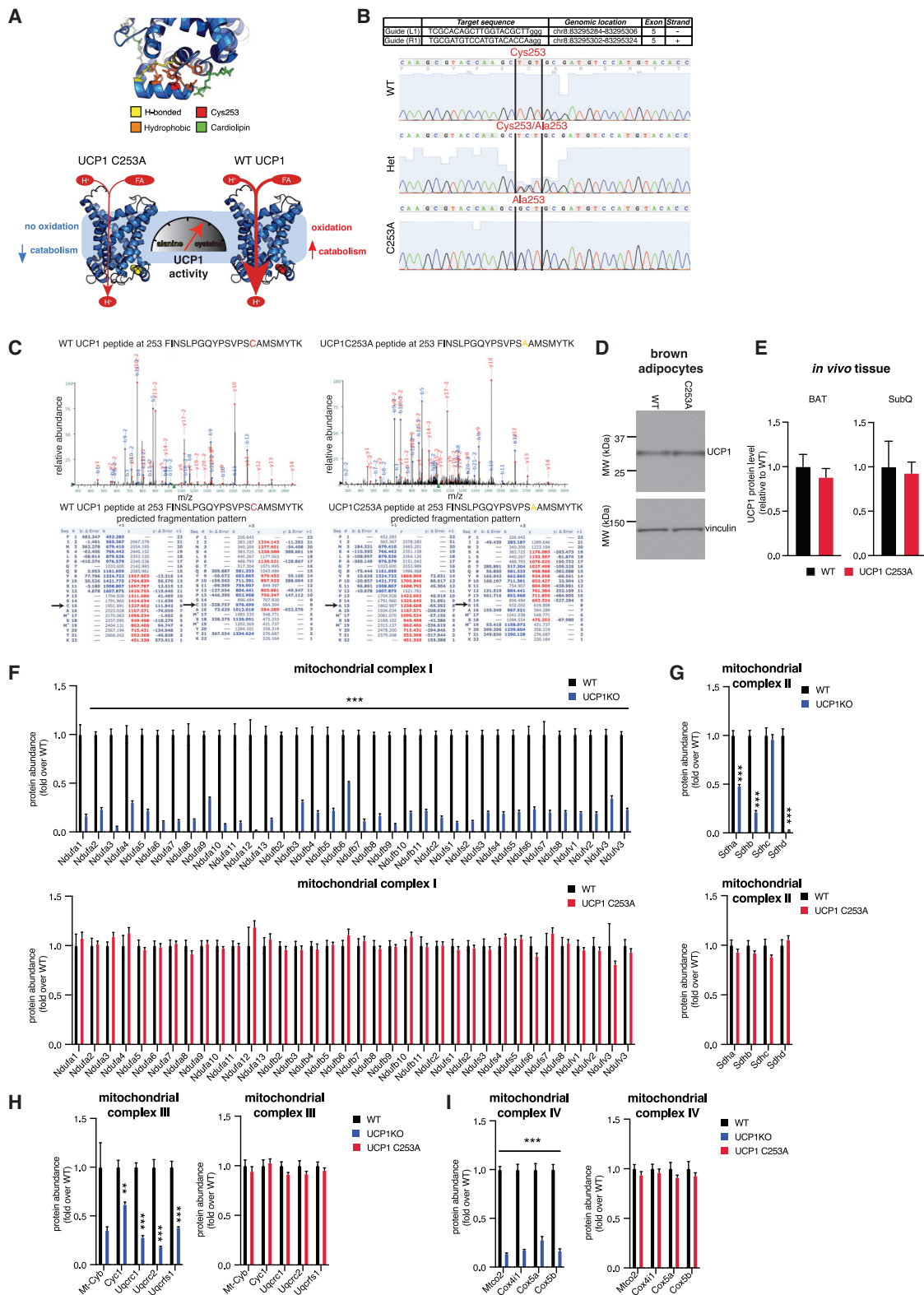
Figure 1. Mutation of UCP1 C253 does not deplete the UCP1 catabolic machinery

(A) Top: structure of human UCP1 modeled on the homologous mitochondrial ATP/ADP carrier (AAC) crystal structure showing the location of a hydrophobic pocket containing UCP1 C253. The model shows that C253 resides at an interface between two helices that stabilize the closed state of UCP1 and that its

The importance of UCP1 in the regulation of thermogenesis *in vivo* has been demonstrated by genetic loss of function; UCP1 knockout (UCP1KO) mice display severe sensitivity to cold temperatures and lack a thermogenic response to BAT adrenoreceptor agonism (Enerbäck et al., 1997). Moreover, it has been suggested that basal UCP1 activity contributes to protection against obesity. These conclusions are based on the observation that UCP1KO mice exhibit sensitivity to diet-induced weight gain at thermoneutrality, but not at room temperature (Enerbäck et al., 1997; Feldmann et al., 2009). However, it has now been determined that loss of UCP1 causes depletion of most components of the mitochondrial electron transport chain (ETC) in BAT (Kazak et al., 2017b; Mills et al., 2021). Therefore, interpretation of phenotypes of UCP1KO mice are confounded and are attributable to both the depletion of the ETC as well as to loss of UCP1 protein per se. This finding underscores the need for a genetic model that specifically disrupts UCP1 activation, without depleting the ETC, to assess its importance in thermogenesis, physiology, and metabolic disease.

Brown and beige adipocyte thermogenesis is regulated by reactive oxygen species (ROS) that initiate thermogenesis by reversible covalent modification of protein cysteine residues (Chouchani et al., 2016). Robust activation of adipocyte thermogenesis *in vivo* results from genetic manipulations that elevate cysteine oxidation in adipose tissue (Chouchani et al., 2016, 2017; Han et al., 2016; Kazak et al., 2017b; Lee et al., 2016; Lettieri Barbato et al., 2015; Mills et al., 2018; Ro et al., 2014; Schneider et al., 2016). Similarly, pharmacological elevation of ROS (e.g., superoxide and hydrogen peroxide) or elevation of protein thiol oxidation is sufficient to drive rapid and robust activation of adipocyte thermogenesis (Chouchani et al., 2017; Han et al., 2016; Kazak et al., 2017b; Lee et al., 2016; Schneider et al., 2016; Shi et al., 2021). Conversely, adipose tissue thermogenesis initiated by physiologic interventions (e.g., cold exposure) depends on endogenously produced cysteine-reactive ROS, most probably hydrogen peroxide (Chouchani et al., 2016; Mills et al., 2018; Sanchez-Alavez et al., 2014; Sanchez-Alavez et al., 2013; Shi et al., 2021).

Building on these discoveries, we have reported that thermogenic ROS reversibly modify a regulatory site (C253) on UCP1, which elevates UCP1-dependent respiration (Chouchani et al., 2016). Structural modeling suggests that UCP1 C253 maps to a hydrophobic interface that stabilizes the inactive conformation of the protein (Chouchani et al., 2016). Modeling covalent modifications on this site, such as to a sulfenic acid by reaction with hydrogen peroxide, are predicted to disrupt this interface and drive a conformational change to increase UCP1 activity. Thus, UCP1-dependent thermogenesis may be tuned through modification of C253, which destabilizes the inactive structural conformation (Figure 1A). In this work, we generate a mouse model in which the regulatory C253 site on UCP1 is mutated to an alanine (UCP1 C253A mouse) to examine its relevance in regulating energy homeostasis and metabolic disease.

RESULTS

The UCP1 C253A mouse: An *in vivo* model for selective disruption of UCP1 activation

Using CRISPR, we generated a mouse model with an individual point mutation on UCP1 at the redox-regulated residue C253, which has been mutated to an alanine (UCP1 C253A) (Figures 1B, 1C, and S1A). Modification of C253 is thought to destabilize the inactive conformation of UCP1. On this basis, mutation to alanine will desensitize UCP1 to activation (Figure 1A). We first examined expression and stability of the C253A form of UCP1 *in vitro* in both brown adipocytes differentiated from stromal vascular fraction (SVF) cells and *in vivo* in BAT. These data indicate that UCP1 C253A protein expression is comparable to wild-type (WT) levels (Figures 1D and 1E). Critically, quantitative proteomics of BAT from WT, UCP1KO, and UCP1 C253A mice demonstrated that unlike UCP1KO BAT, UCP1 C253A BAT maintained expression of the full repertoire of mitochondrial metabolic proteins at WT levels under standard housing conditions (Figures 1F–1I and S1B). We observed no consistent difference in mRNA or protein expression of other UCP isoforms in BAT or subcutaneous white adipose tissue (subQ) between genotypes (Figures S1C–S1F). Therefore, the UCP1 C253A mouse has a specific disruption of UCP1 C253 without additional depletion of the catabolic machinery in BAT.

Loss of UCP1 C253 impairs the thermogenic response in brown adipocytes and BAT *in vivo*

We began by characterizing the metabolic physiology of UCP1 C253A mice under standard housing conditions. In this setting, WT and UCP1 C253A mice had identical body mass and body mass composition (Figures 2A–2E). We then exposed UCP1 C253A mice to a range of acute thermogenic stimuli to elicit differing extents of UCP1 activation, while monitoring energy expenditure and metabolic parameters using indirect calorimetry (Figures 2C, 2F–2J, S1G–S1P, and S2A–S2D). Absent thermal challenge (thermoneutrality, TN, 29°C) or with modest thermal stress (room temperature, RT, 22°C), both male and

---

oxidation could destabilize the closed state, sensitizing UCP1 to activation by fatty acids (FA). Bottom: proposed model suggesting that redox modification of C253 sensitizes UCP1 to activation by adrenergic stimulation and FA-mediated activation.

(B) Sequencing UCP1 C253 locus of WT, UCP1C253A, and heterozygote mouse.

(C) Representative MS/MS fragment spectrum determining the locus containing amino acid 253 from WT and UCP1 C253A BAT. The spectra illustrate fragment ion assignments: b ions extending from the amino terminus (blue) and y ions extending from the carboxyl terminus (red). Arrow highlights high-confidence assignment of cysteine at position 253 in WT BAT and alanine at position 253 in UCP1 C253A BAT. Fragment ion assignments from both singly (+1) and doubly (+2) charged peptides are shown, including mass error measurements (Δ error).

(D) Immunoblot analysis of UCP1 protein in brown adipocytes isolated and differentiated from SVF from WT and UCP1 C253A BAT. Data are representative of 5 experiments.

(E) UCP1 protein abundance in WT and UCP1 C253A BAT (left) and subQ (right) (n = 5).

(F–I) Protein abundance differences between WT and UCP1 C253A and WT and UCP1KO BAT of mitochondrial respiratory chain proteins (WT [UCP1KO C253A control], WT [UCP1KO control]; UCP1 C253A n = 5; UCP1KO n = 4).

**p < 0.01, ***p < 0.001 (two-tailed Student's t test for pairwise comparisons). Data are mean ± SEM.
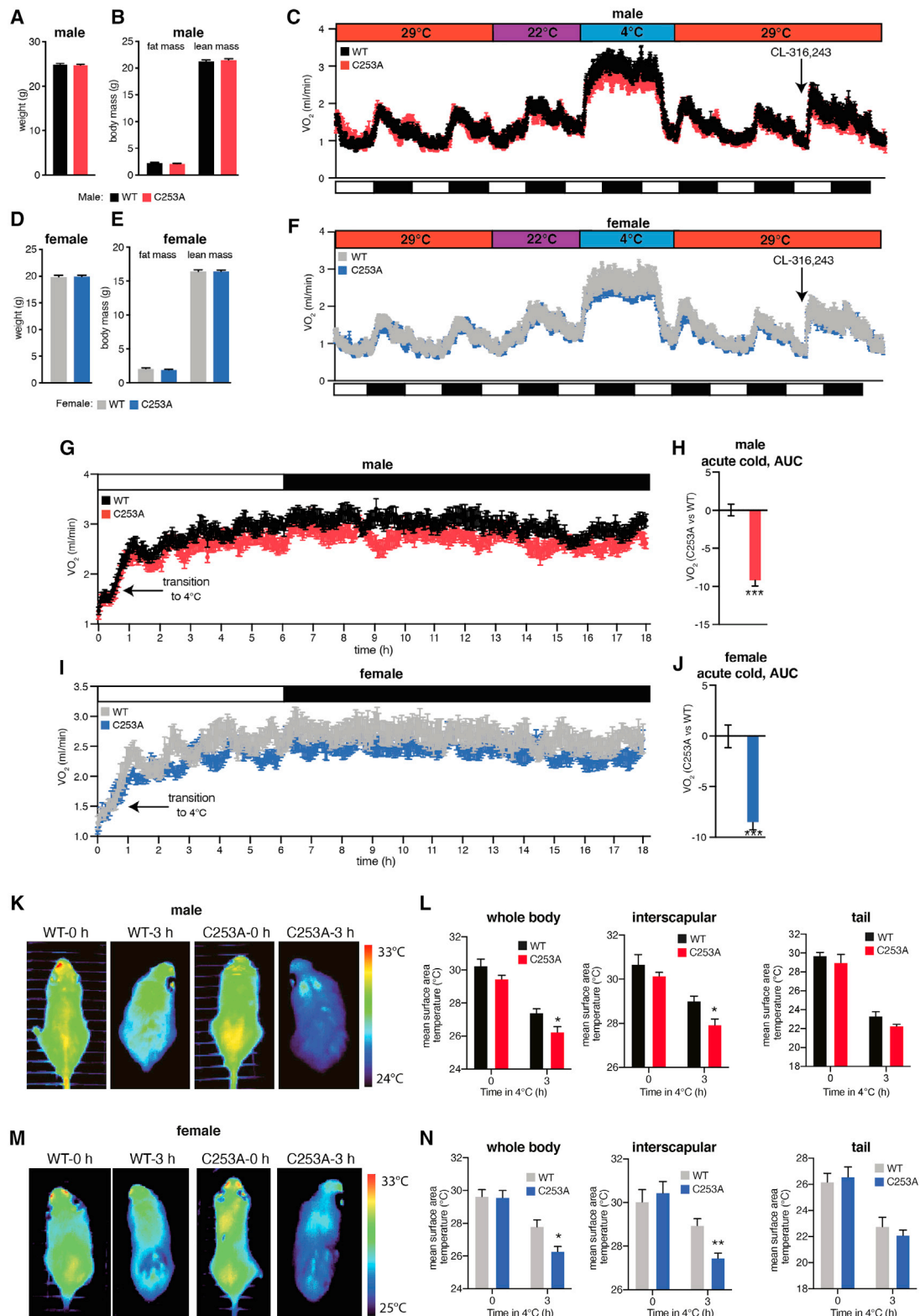
Figure 2. UCP1 C253A mice are thermogenically compromised upon cold exposure

(A and D) Body mass of male (A) and female (D) WT and C253A mice (male: WT n = 59, UCP1 C253A n = 56; female: WT n = 41, UCP1 C253A n = 50).

(B and E) Body composition of male (B) and female (E) WT and C253A mice (male: WT n = 59, UCP1 C253A n = 56; female: WT n = 41, UCP1 C253A n = 50).

female WT and UCP1 C253A mice displayed comparable rates of oxygen consumption (VO_2), CO_2 release (VCO_2), and energy expenditure (Figures 2C, 2F, and S1G–S1J). However, upon exposure to cold (4°C), both male and female C253A mice exhibited significantly lower VO_2 consumption (Figures 2G–2J), energy expenditure (Figures S1K and S1L), and VCO_2 production (Figures S1M and S1N) compared with WT mice. Interestingly, UCP1 C253A mice exhibited comparable responses to β3-adrenoreceptor agonism by CL-316,243 (Figures S1O and S1P), an established activator of adipose tissue thermogenesis (Bloom et al., 1992; Granneman et al., 2003; Himms-Hagen et al., 1994). However, isolated brown adipocytes had a blunted respiratory response to norepinephrine (NE), which stimulates both α and β-adrenoreceptors, and requires ROS generation for full activation of UCP1-dependent thermogenesis (Chouchani et al., 2016) (Figure S1Q). These findings contrast with UCP1KO mice that are both sensitive to acute cold challenge and consume less oxygen after treatment with a β3-adrenergic-receptor agonist (Enerbäck et al., 1997). This discrepancy could be due in part to additional ROS-producing factors, such as succinate, that are generated in response to cold exposure, but not β3-agonism (Mills et al., 2018). Following all *in vivo* stimuli noted above, no difference in food intake (Figures S2A and S2B) or movement (Figures S2C and S2D) was observed between genotypes.

Next, we exposed male and female WT and UCP1 C253A mice to cold, as above, and monitored body temperature using infrared thermography (Crane et al., 2014). We observed a significant decrease in dorsal surface temperature, both in the interscapular and entire body area, but not the tails, of UCP1 C253A male and female mice (Figures 2K–2N). The degree of hypothermia observed was comparable with that previously reported in BAT depletion models (Lowell et al., 1993) and depletion of other thermogenic pathways in BAT/beige fat such as creatine-dependent thermogenesis (Kazak et al., 2017a). These data correlate strongly with the observed effect on VO_2 and energy expenditure (Figures 2C and 2F–2J), demonstrating that, in response to cold exposure, the thermogenic response is significantly blunted in UCP1 C253A mice.

Loss of UCP1 C253 does not affect fat mass accumulation or energy expenditure upon obesogenesis

UCP1 activity has been implicated in regulation of obesity based on findings in the UCP1KO mouse, a model with the substantial caveats described above. Therefore, we next investigated the role of UCP1 C253 in modulation of whole-body energy expenditure during diet-induced obesity (DIO). To do so, male and female UCP1 C253A mice were housed at TN and subjected to an *ab libitum* high-fat, high-sucrose (HFHS) diet for 12 weeks. WT

and UCP1 C253A mice gained considerable and indistinguishable weight and fat mass upon HFHS feeding (Figures 3A–3F), and food intake between groups was identical (Figures 3G and 3H). We additionally applied the energy balance method (Goldgof et al., 2014; Ravussin et al., 2013) to assess whole-body energy expenditure and found no difference between genotypes (Figures 3I–3N). The phenotypes described above were also observed in mice subjected to DIO when housed at RT (Figures S5G–S5R). Histological assessment of BAT and subQ following HFHS diet revealed no difference in adiposity/adipocyte size between genotypes (Figures S2E–S2L). Minimal differences in transcripts related to UCP1 and the thermogenic program were observed BAT and subQ of WT and UCP1 C253A mice following HFHS feeding (Figures S2M–S2R).

Remarkably, despite the lack of adiposity difference between genotypes, male C253A mice exhibited significantly more glucose intolerance, compared with WT mice, following HFHS feeding (Figure 3O). Of note, glucose intolerance was identical between WT and UCP1 C253A female mice (Figure 3P). We therefore examined whether glucose uptake into BAT differs between male genotypes. To do so, we injected mice with $^{13}C_6$-glucose and traced glucose uptake and metabolism in BAT, muscle, and liver (Figures S2S–S2W). Interestingly, we found that glucose uptake initially increased into UCP1 C253A BAT (Figure S2S), but catabolism of glucose through the lower portion of glycolysis was significantly compromised (Figure S2T). These data suggest that glucose metabolism is impaired in BAT of UCP1 C253A mice, which could contribute to the glucose insensitivity observed following HFHS feeding. Glucose uptake and metabolism was unaltered in liver of UCP1 C253A mice (Figures S2U and S2V), and a small decrease in metabolic flux through glycolysis was observed in muscle of UCP1 C253A mice (Figures S2U and S2W). It should be noted that these experiments were performed in chow-fed mice, while the glucose intolerance phenotype was observed in mice on a HFHS diet. It could therefore be expected that the above-described inhibition of glucose catabolism in BAT and muscle of UCP1 C253A mice would be exacerbated following HFHS diet.

Sexually dimorphic regulation of adipose tissue inflammation by UCP1 C253

We next explored the role of UCP1 C253 on adipose tissue physiology more broadly. To do so, we first performed proteomic analysis of adipose tissues from both male and female mice following HFHS feeding to identify biological processes that are altered in the absence of UCP1 C253. We focused first on subQ WAT, which is known to remodel substantially upon DIO and to mediate obesity-related pathologies. SubQ WAT from UCP1 C253A male mice exhibited increased protein abundance

(C and F) VO_2 of male (C) and female (F) WT and C253A mice at the depicted temperatures and with an intraperitoneal (i.p.) injection of CL-316.234 (1 mg/kg) (male: WT n = 17, UCP1 C253A n = 14; female: WT n = 16, UCP1 C253A n = 14).

(G and I) Zoom in of VO_2 of male (G) and female (I) WT and C253A mice upon transition to 4°C (male: WT n = 17, UCP1 C253A n = 14; female: WT n = 16, UCP1 C253A n = 14).

(H and J) % change in area under the curve of acute cold VO_2 of male (H) and female (J) WT and UCP1 C253A mice (male: WT n = 17, UCP1 C253A n = 14; female: WT n = 16, UCP1 C253A n = 14).

(K and M) Representative infrared images of WT and UCP1 C253A male (K) and female (M) mice following 3-h cold exposure.

(L and N) Surface temperature of the entire body, interscapular BAT area, or tail of WT and UCP1 C253A mice following 3-h cold exposure. Surface temperature is calculated as the average of the highest 50% area of the region of interest (male: WT n = 6, UCP1 C253A n = 7; female: WT n = 4, UCP1 C253A n = 6).

*p < 0.05, **p < 0.01, ***p < 0.001 (two-tailed Student's t test for pairwise comparisons). Data are mean ± SEM.
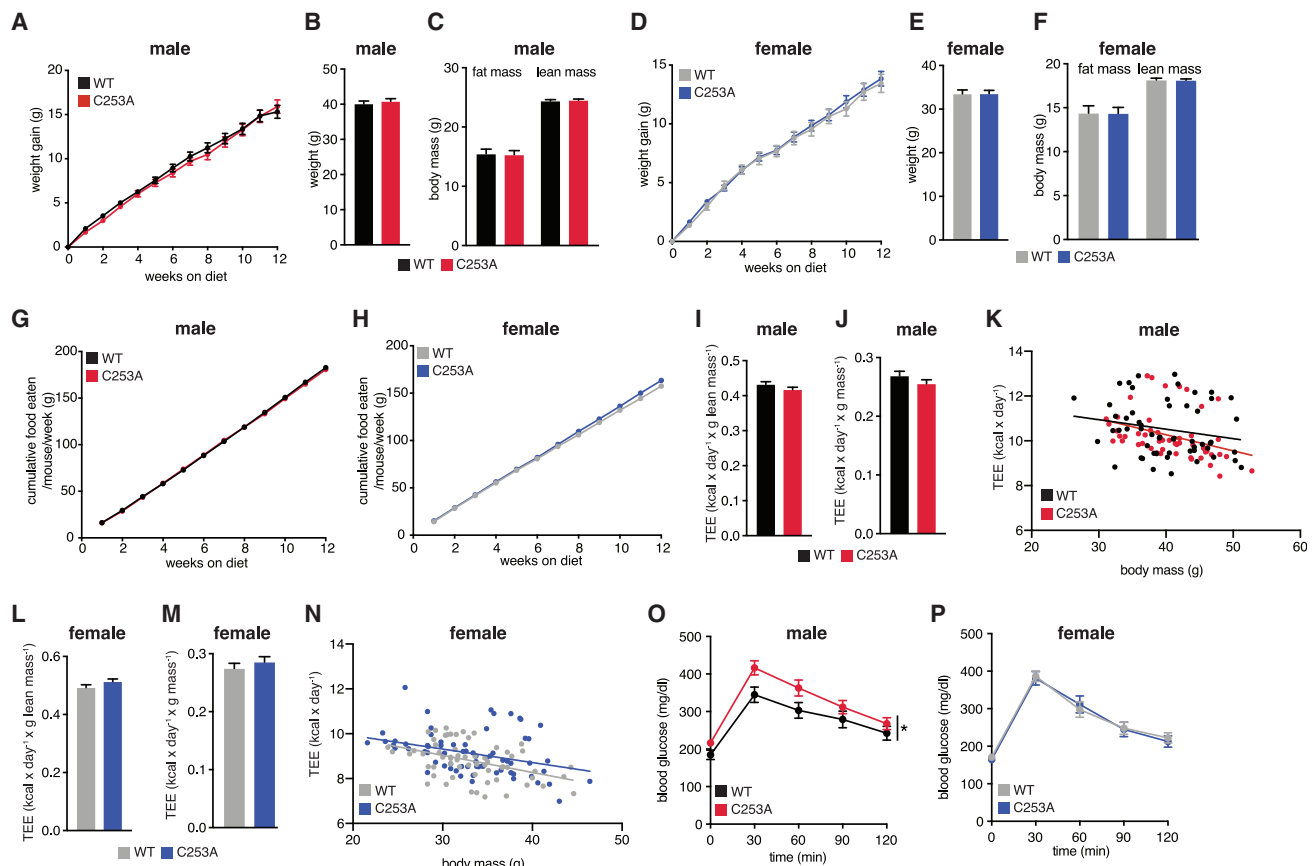
Figure 3. UCP1 C253A mice have similar adiposity to WT upon HFD

(A and B) Change in body mass (A) and final weight (B) of male mice during HFHS feeding (WT n = 55, UCP1 C253A n = 50).

(C) Body composition of male mice following 12 weeks HFHS feeding (WT n = 55, UCP1 C253A n = 50).

(D and E) Change in body mass (D) and final weight (E) of female mice during HFHS feeding (WT n = 41, UCP1 C253A n = 50).

(F) Body composition of female mice following 12 weeks HFHS feeding (WT n = 41, UCP1 C253A n = 50).

(G and H) Cumulative food intake in male (G) and female (H) male mice throughout 12 weeks HFHS feeding (male: WT n = 55, UCP1 C253A n = 46; female: WT n = 41, UCP1 C253A n = 50).

(I–N) Cumulative whole-body energy expenditure of male (I–K) or female (L–N) mice over 12 weeks HFHS feeding, determined as described in STAR Methods (male: WT n = 55, UCP1 C253A n = 50; female: WT n = 41, UCP1 C253A n = 50).

(O and P) i.p. glucose tolerance test in male (O) and female (P) mice following 12 weeks HFHS feeding (male WT and C253A n = 19, female: WT n = 20, UCP1 C253A n = 19).

*$p < 0.05$ (two-tailed Student's t test for pairwise comparisons, one-way ANOVA for multiple comparisons involving independent variable, two-way ANOVA for multiple comparisons involving two independent variables, ANCOVA for K and N). Data are mean ± SEM.

of major drivers of inflammation, compared with WT, as determined by unbiased pathway analysis (Figures 4A–4E; Table S1). A significant increase in abundance of proteins that regulate immune cell phagocytosis (Figure 4B), antigen processing and presentation (Figure 4C), and neutrophil-mediated immunity (Figure 4D) was observed in male UCP1 C253A subQ WAT. Fc-receptor-mediated phagocytosis involves the ligation of the Fc receptor, which is found on the surface of many immune cells but notably on macrophages and neutrophils, to antibody coated antigens (Aderem and Underhill, 1999). Proteins involved in phagocytosis (Figure 4A) and immunoglobulins (Figure 4E) were upregulated male UCP1 C253A subQ WAT, including several actin remodeling proteins (Figure 4B), which are central for macrophage and neutrophil phagocytosis. Interestingly, neutrophils are a major cell type that play a role in phagocytosis, and

proteomic analysis also indicated an increase in neutrophil activity in male UCP1 C253A subQ WAT (Figure 4D). Neutrophil activation following phagocytosis of antigens initiates a local immune response and inflammation, mainly via the production of ROS and the release of proteases and anti-microbial peptides founds within their intracellular granules (Mócsai, 2013). Indeed, in male UCP1 C253A WAT, we observed an increase in major protein drivers of neutrophil activation including Ncf (neutrophil cytosol factor)1 and Ncf4, two subunits of neutrophil NADPH oxidase, (Figures 4B and 4E) as well as the lysosomal proteins Hexb (Beta-hexosaminidase subunit beta) and Lyz2 (Lysozyme C-2; Figures 4D and 4E). Importantly, phagocytic NADPH oxidase activity has been linked with damaging oxidative stress in patients with hyperinsulinemia (Fortuno et al., 2006). More generally, neutrophils have been directly implicated in the
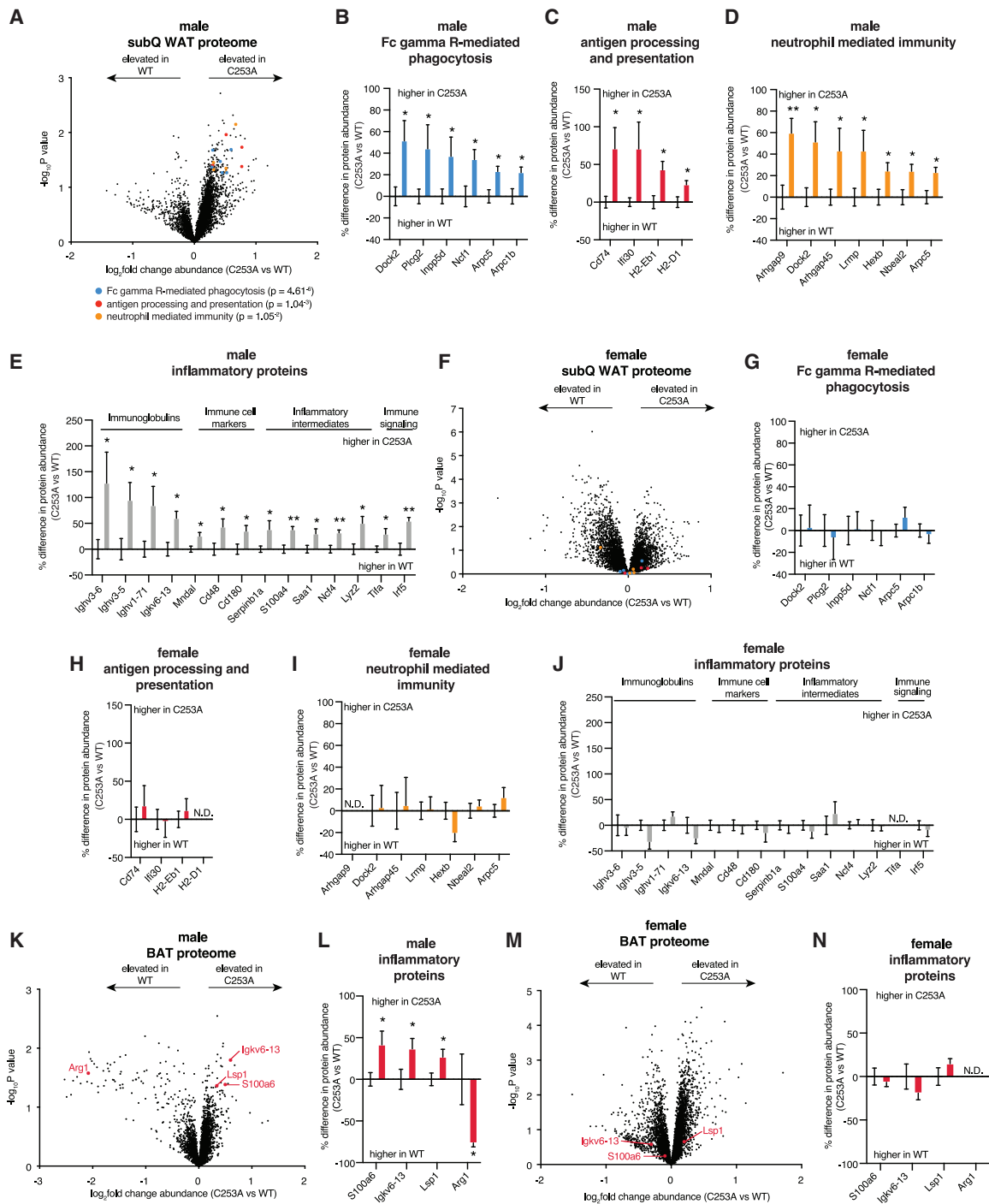
Figure 4. Mutation of UCP1 C253A promotes an inflammatory response in subQ and BAT of male, but not female, mice

(A) Protein abundance differences between male WT and UCP1 C253A subQ following 12 weeks HFHS feeding. Top pathways enriched in proteins exhibiting >20% increase between genotypes highlighted (WT n = 7; UCP1 C253A n = 5).

(B–E) Protein abundance differences of top enriched pathways (B–D) or established pro-inflammatory proteins (E) between WT and UCP1 C253A subQ following 12 weeks HFHS feeding (WT n = 7; UCP1 C253A n = 5).

(F) Protein abundance differences between female WT and UCP1 C253A subQ following 12 weeks HFHS feeding. Top pathways found to be enriched in proteins exhibiting >20% increase between WT and UCP1 C253A males in (A) are highlighted; (n = 8).

(G–J) Protein abundance differences of top enriched pathways (G–I) or established pro-inflammatory proteins (J) between WT and UCP1 C253A female subQ following 12 weeks HFHS feeding (n = 8).

(legend continued on next page)

pathogenesis of high-fat-diet-induced glucose insensitivity, largely because of the release of intracellular inflammatory agents (Talukdar et al., 2012).

As well as stimulating immune cell activation, phagocytosis is also required for the uptake of extracellular antigens, which are then processed and presented to cells of the adaptive immune system to initiate their activation. Along these lines, we also observed increased abundance of proteins that mediate antigen processing and presentation in WAT from C253A male mice (Figure 4C). These proteins are all associated with major histocompatibility complex (MHC) class II, which is found exclusively on professional antigen-presenting cells including macrophages, dendritic cells, and B cells. We also observed increased abundance of several macrophage and dendritic cell markers such as CD74, CD48, and CD180 (Figure 4E). Notably, CD180 is part of a cell surface receptor complex associated with Toll-like receptor 4, (TLR4). Ligation of TLR4 is known to occur during obesity and leads to the activation of NFκB, a major regulator of inflammation (Cani et al., 2007). In line with this, we observed increased abundance of other components of this pathway including Irf5 (interferon regulatory factor 5) and Tifa (TRAF-interacting protein with FHA-domain-containing protein A; Figure 4E). Systemic activation of NFκB is associated with glucose intolerance, and NFκB blockade is protective in this context (Eldor et al., 2006). Furthermore, NFκB activation results in the production of a range of pro-inflammatory intermediates such as acute phase proteins, cytokines, chemokines, and danger associated molecular patterns (DAMPs). We detected elevated abundance of several such intermediates, including the DAMP S100a4 and the acute phase protein Saa1 (serum amyloid A1; Figure 4E). Both S100a4 (Anguita-Ruiz et al., 2020; Arner et al., 2018) and Saa1 (Scheja et al., 2008; Yang et al., 2006) are hallmarks of glucose intolerance.

We next analyzed subQ WAT of female UCP1 C253A mice following HFHS intervention. To our surprise, the pathogenic inflammatory pathways significantly upregulated in the subQ WAT of male C253A mice were entirely unchanged in the corresponding female tissues (Figures 4F–4J; Table S1). Instead, the subQ of female UCP1 C253A mice was enriched in proteins that regulate the extracellular matrix (ECM; Figures S3A and S3B). Remodeling of the ECM is required for healthy adipose tissue expansion, in part by allowing the formation of new blood vessels (Sun et al., 2013). We also observed a significant increase in proteins associated with protein catabolism (Figure S3C) and mitosis (Figure S3D) suggesting an overall growth/expansion phenotype in the subQ of female UCP1 C253A mice following HFHS diet. Furthermore, several pathways and proteins that contribute to inflammation were significantly downregulated. These included complement system proteins (Figure S3E), cholesterol metabolic proteins (Figure S3F), mast cell secretory granule proteins, and immune cell signaling and antigen-processing and presentation-related proteins (Figure S3G) (Engström et al., 2005; Lim et al., 2013; Wlazlo et al., 2014; Zewinger et al., 2020).

Together these data demonstrate a fundamental sex-dependent regulation of WAT inflammation by UCP1 C253. In males, UCP1 C253 strongly antagonizes immune cell phagocytic markers, antigen processing and presentation markers, and the production of several major inflammatory drivers of metabolic disease. In female WAT, these pathways were either unchanged or downregulated in UCP1 C253A mice. This sex-dependent inflammatory response coincides with a male-selective dependence on UCP1 C253 for maintenance of glucose sensitivity upon high-fat feeding (Figures 3O and 3P).

Based on the findings above, we next determined whether the sex-dependent regulation of WAT inflammation by UCP1 C253 was present in mice absent an obesogenic challenge. We performed proteomic assessment of the subQ of WT and C253A male mice under standard housing conditions on chow diet (Figure S3H; Table S2). Proteins that were significantly upregulated in WAT of male C253A mice following HFHS feeding were not differentially expressed on chow diet (Figures S3H–S3L; Table S2). However, we did observe alterations in certain inflammatory intermediates (Figure S3M); these include the DAMPs S100a1 and S100a13, and the transcription factor CCAAT enhancer binding protein beta (Cebpb), which is critical for macrophage function and regulates several inflammatory genes including several cytokines and acute phase proteins. Taken together, our findings demonstrate that UCP1 C253 antagonizes WAT inflammation in male, but not female mice, particularly in an obesogenic context.

Inflammatory remodeling in BAT upon loss of UCP1 C253 in male, but not female, mice

We additionally identified sex-specific proteome-wide alterations in BAT of male UCP1 C253A mice (Figures 4K and 4L; Table S3). The major upregulated proteins in BAT of UCP1 C253A male mice were associated with inflammation (Figures 4K and 4L). These include the immune cell protein Lsp1 (lymphocyte specific protein 1) and the DAMP S100a6. Conversely, among the most downregulated proteins was Arg1 (arginase1), a critical marker of anti-inflammatory macrophages (Figure 4L). We also observed a significant downregulation of several metabolic pathways that are linked to regulation of inflammation, including metabolic enzymes involved in S-Adenosyl methionine (SAMe) and amino acid catabolism (Figures S4A–S4C), as well as urea cycle metabolism (Figures S4A and S4D). Moreover, under standard chow diet feeding conditions, male UCP1 C253A BAT exhibited an elevation in proteins and pathways associated with inflammation including neutrophil-mediated immunity, leukocyte migration and complement (Figures S3N–S3R; Table S2).

The above-described changes were not observed in females (Figures 4M, 4N, and S4E–S4H; Table S3). Instead, proteins involved in regulating mitochondrial translation, substrate catabolism, and thermogenesis, including a number of ETC components, were significantly upregulated in the BAT of female UCP1 C253A mice (Figures S4I–S4L; Table S3). It is possible

(K and M) Protein abundance differences between male (K) and female (M) WT and UCP1 C253A BAT following 12 weeks HFHS feeding with inflammatory proteins highlighted (n = 8).

(L and N) Protein abundance differences of established pro-inflammatory proteins between WT and UCP1 C253A male (L) and female (N) BAT following 12 weeks HFHS feeding (n = 8).

*p < 0.05, **p < 0.01 (two-tailed Student's t test for pairwise comparisons). Data are mean ± SEM.

that in the absence of UCP1 C253, female mice possess the capacity to upregulate alternative modes of substrate catabolism, such as increased carbon and fatty acid oxidation (Figures S4J–S4L). Finally, proteins related to the NLRP3 inflammasome, an important pro-inflammatory signaling hub, were downregulated in BAT of female UCP1 C253A mice (Figure S4M).

Sexually dimorphic regulation of adipose tissue immune cell populations by UCP1 C253

Our proteomic analyses suggested a fundamentally remodeled immune cell population in male, but not female, adipose tissues in the absence of UCP1 C253. We next directly examined whether immune cell populations and inflammatory proteins in these tissues could be regulated by UCP1 C253 following initiation of obesogenesis. Flow cytometry analysis revealed an increase in absolute numbers of CD3$^+$ cells in the subQ of male UCP1 C253A mice (Figures 5A and S8). This was attributable to an increase in abundance of CD8$^+$ cytotoxic T cells (Figure 5B). Increased numbers of CD8$^+$ T cells has been observed during obesity, and depletion of these cells has been shown to limit macrophage infiltration to WAT and to decrease inflammation and glucose intolerance (Nishimura et al., 2009). Furthermore, we identified an increased abundance of inflammatory macrophages (Figures 5C and 5D), perhaps as a consequence of the increased number of CD8$^+$ T cells, in the subQ WAT of male UCP1 C253A mice. A similar increase in myeloid cells was observed in BAT from male UCP1 C253A mice (Figures 5E and 5F). Notably, the abundance of both CD3$^+$ and CD8$^+$ cells was decreased in the subQ of female UCP1 C253A mice (Figures 5A and 5B), while the numbers of macrophages in BAT and subQ remained unchanged between genotypes in females (Figures 5C–5F).

We next examined the expression of established pro- and anti-inflammatory molecules following obesogenic feeding. We observed a significant increase in expression of the pro-inflammatory cytokine *Il1b* in the BAT and subQ WAT of male UCP1 C253A mice (Figures 5G and 5H). We additionally detected increased expression of *Tnf* and the chemokine *Ccl2* in the BAT of male UCP1 C253A mice (Figure 5H). CCL2 is a chemotactic factor for macrophages and inflammatory monocytes and is known to contribute to the infiltration of these cells into adipose tissues during DIO and to play a role in the progression of glucose intolerance (Kamei et al., 2006; Kanda et al., 2006). Conversely, we observed a significant decrease in the expression of the anti-inflammatory cytokine *Il10* (Figures 5G and 5H). These inflammatory phenotypes were sex dependent; the expression of these intermediates was either unchanged or significantly downregulated in subQ and BAT from female UCP1 C253A mice (Figures 5G and 5H). A similar sex-specific inflammatory phenotype was observed in C253A mice at RT upon obesogenesis (Figures S5S and S5T). This phenotypic switch to a pro-inflammatory profile has been extensively linked with obesity-associated inflammation, pathology, and progression of type 2 diabetes (T2D) (Eldor et al., 2006; Lumeng et al., 2007; Maedler et al., 2002; Spranger et al., 2003). Indeed, IL-1β antagonists and NSAIDs have shown beneficial effects in type 2 diabetic patients (Fleischman et al., 2008; Goldfine et al., 2010; Goldfine et al., 2008; Koska et al., 2009; Larsen et al., 2007, 2009). On the other hand, the anti-inflammatory

cytokine IL-10 has been suggested to limit diet-induced inflammation and glucose intolerance in mouse models (Hong et al., 2009). In sum, these data illustrate a role for UCP1 C253 in the regulation of adipose tissue immune cell and inflammatory homeostasis in male mice.

Systemic inflammatory remodeling in male UCP1 C253A mice

We next determined if loss of UCP1 C253 could exert effects systemically in tissues that do not express UCP1. We explored the effect of C253 mutation on inflammation in the epididymal white adipose tissue (epi) and liver following HFHS feeding, two tissues known to remodel substantially following obesogenic intervention. Interestingly, histological analysis of epi WAT showed an increase in abundance of crown-like structures in male, but not female, UCP1 C253A mice (Figure S5A). The expression of several inflammatory markers was increased in the liver of male, but not female, UCP1 C253A mice (Figures S5B–S5F; Table S4). This included cytokines, chemokines, several immunoglobulins, B-cell-receptor-associated protein 29 (Bcap29), which plays a role in B cell receptor signaling, and lipopolysaccharide-induced TNF factor (Litaf) (Figures S5B–S5F). A similar inflammatory phenotype was observed in the livers of male, but not female, UCP1 C253A upon DIO at RT (Figure S5U). Together, these data indicate that loss of UCP1 C253 exerts systemic inflammatory effects in non-UCP1 expressing tissues.

Disrupted redox homeostasis and mtDNA damage and release drive sex-dependent inflammation regulated by UCP1 C253

We next explored how loss of UCP1 C253, which is selectively expressed in brown and beige fat, could affect both local and systemic inflammation. Because of the interdependence between ROS and UCP1 activity, we hypothesized that in the absence of UCP1 C253 to respond to, and decrease, local ROS levels (Chouchani et al., 2016; Ukropec et al., 2006), BAT mitochondria would be exposed to elevated ROS-driven macromolecular oxidation. Oxidation of macromolecules of mitochondrial origin (such as mitochondrial mtDNA [mtDNA]), which can be released into the circulation, are known mediators of systemic inflammation (Collins et al., 2004; Oka et al., 2012; Shimada et al., 2012; Zhang et al., 2010). These factors could explain some of the systemic consequences of compromised UCP1 activity.

We first examined whether loss of UCP1 C253 affected BAT redox homeostasis by systematically quantifying the reversible oxidation state of protein cysteine residues, which are highly sensitive to alterations in local ROS levels. To do so, we used the cysteine-reactive phosphate tag (CPT) methodology (Xiao et al., 2020) to map the cysteine oxidation state across the proteome in BAT (Figures S6A–S6C; Table S4). We determined that the oxidation status of several hundreds of cysteines is altered in C253A BAT compared with WT following HFHS feeding (Figures S6A and S6B). We found a significant enrichment of highly oxidized mitochondrial proteins in BAT from UCP1 C253A mice (Figures S6A and S6C). Furthermore, we found an increase in oxidation of several proteins associated with inflammatory processes including NFκB, MAPK, adipocytokine, and type I
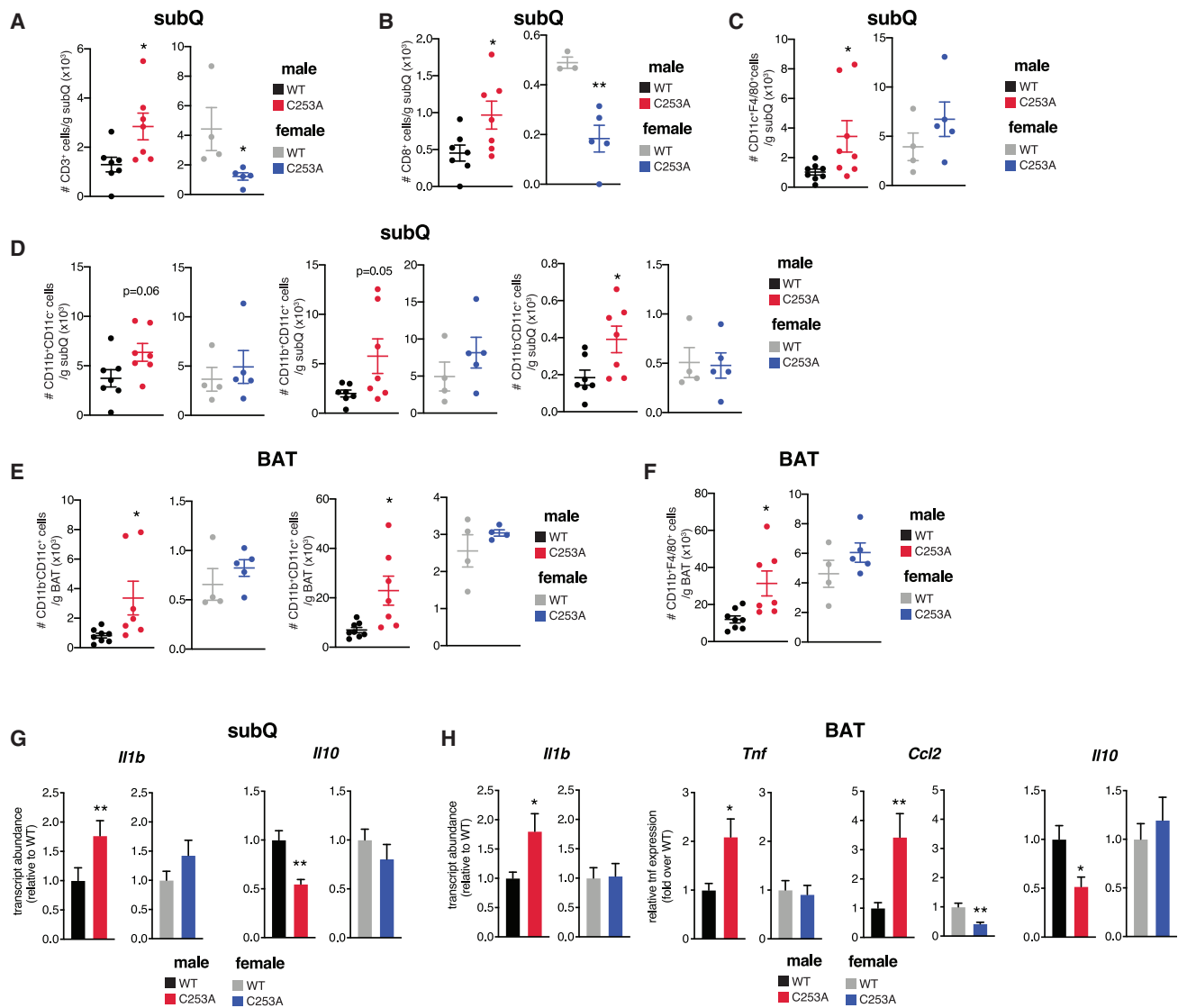
Figure 5. UCP1 C253A controls inflammation and immune cell populations in subQ and BAT in a sex-dependent manner

(A–D) Cell numbers for each indicated population from subQ of male and female WT and UCP1 C253A mice following 12 weeks on HFHS diet (male WT and C253A n = 7; female: WT n = 4, UCP1 C253A n = 5).

(E and F) Cell numbers for each indicated population from BAT of male and female WT and UCP1 C253A mice following 12 weeks on HFHS diet (male: WT n = 8, UCP1 C253A n = 7; female: WT n = 4, UCP1 C253A n = 5).

(G) Relative gene expression of cytokines in subQ from WT and UCP1 C253A mice following 12 weeks on HFHS diet (male: WT n = 9, UCP1 C253A n = 7–9; female: WT n = 8, UCP1 C253A n = 9).

(H) Relative gene expression of inflammatory intermediates in BAT from WT and UCP1 C253A mice following 12 weeks on HFHS diet (male: WT n = 9, UCP1 C253A n = 9; female: WT n = 9, UCP1 C253A n = 8–9).

*p < 0.05, **p < 0.01 (two-tailed Student's t test for pairwise comparisons). Data are mean ± SEM.

interferon signaling (Figure S6A). Based on the observation that loss of UCP1 C253 increased levels of mitochondrial protein oxidation, we examined mtDNA damage, which is a direct consequence of increased mtROS production, and has been implicated in systemic inflammatory pathogenesis. ROS-driven oxidation can damage mtDNA and also drive mtDNA release into the circulation to act as a DAMP to promote an immune response. Remarkably, we observed a significant increase in mtDNA damage in BAT (Figure 6A), and a significant increase

in circulating mtDNA in male, but not female, C253A mice (Figure 6B).

Since ROS-driven macromolecular oxidation in BAT is a direct consequence of loss of UCP1 C253, we next examined whether it was required for systemic tissue inflammation observed during HFHS feeding. To test this, we supplemented the drinking water of WT and UCP1 C253A mice on a HFHS diet with the mitochondria-targeted antioxidant, MitoQ, using an established dosing regimen (Rodriguez-Cuenca et al., 2010) (Figures S6D–S6H).
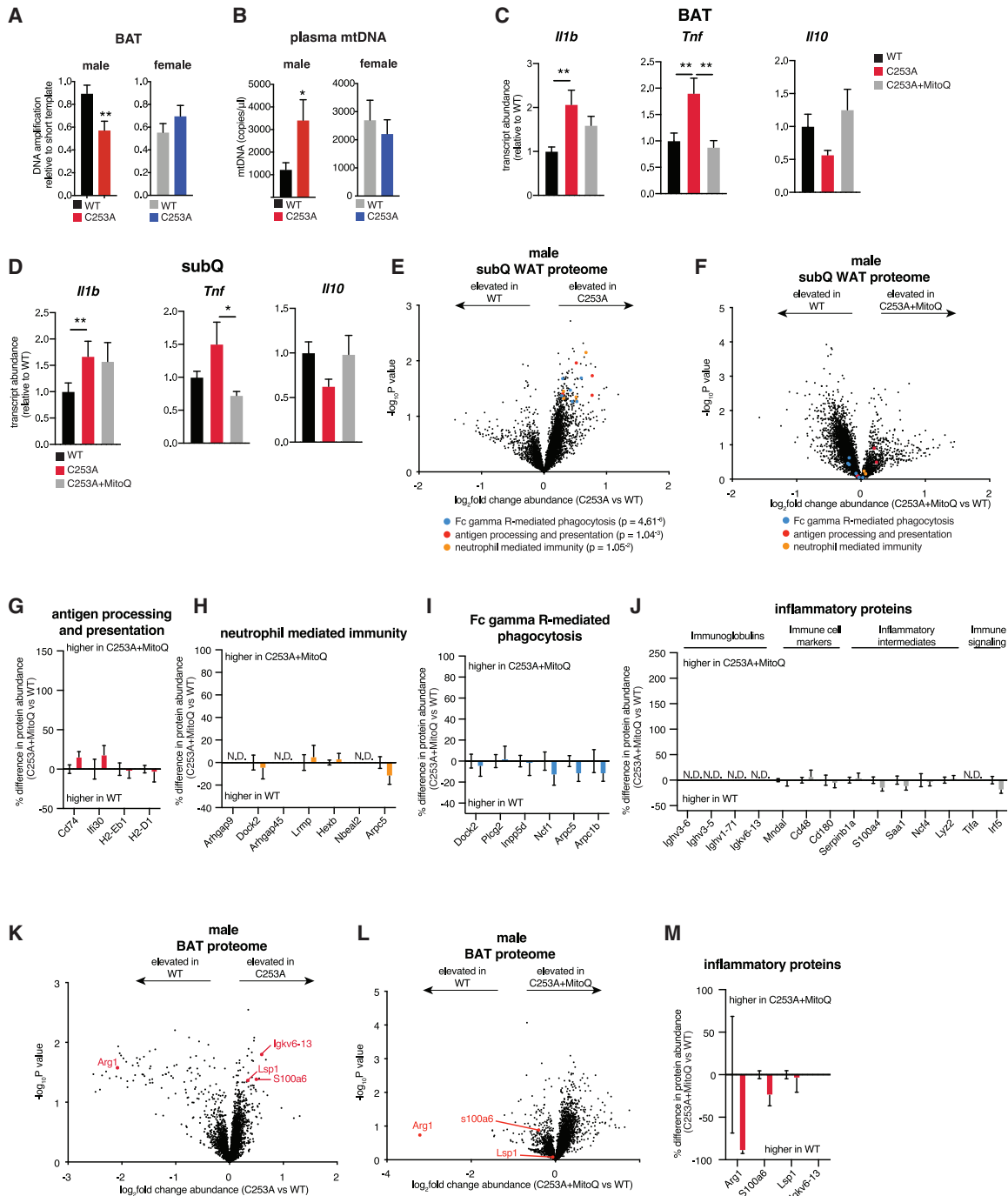
Figure 6. Redox stress in male C253A mice contributes to the observed inflammatory phenotype

(A) mtDNA damage in male and female WT and UCP1 C253A BAT following 12 weeks HFHS feeding (male: WT n = 10, UCP1 C253A n = 10; female: WT n = 11, UCP1 C253A n = 11). See STAR Methods for details.

(B) Plasma mtDNA levels in male and female WT and UCP1 C253A following 12 weeks HFHS feeding (male: WT n = 10, UCP1 C253A n = 10; female: WT n = 11, UCP1 C253A n = 11).

(C) Relative gene expression of inflammatory intermediates in BAT from WT, UCP1 C253A, and UCP1 C253A mice supplemented with MitoQ in drinking following 12 weeks on HFHS diet (n = 9).

(D) Relative gene expression of inflammatory intermediates in subQ from WT, UCP1 C253A, and UCP1 C253A mice supplemented with MitoQ in drinking following 12 weeks on HFHS diet (WT n = 9; UCP1 C253A n = 8–9; UCP1 C253A + MitoQ n = 8–9).

(E) Protein abundance differences between male WT and UCP1 C253A subQ following 12 weeks HFHS feeding. Top pathways enriched in proteins exhibiting >20% change between genotypes highlighted (WT n = 7; UCP1 C253A n = 5). These data are additionally presented in Figure 4A.

(legend continued on next page)

Supplementation with MitoQ in the drinking water resulted in a significant reversal of the signs of inflammation in BAT and subQ observed in C253A mice at both the protein and mRNA level (Figures 6C–6M). We found that inflammatory cytokine expression was renormalized to WT levels upon MitoQ supplementation (Figures 6C and 6D). We next assessed the proteomes of subQ WAT and BAT from WT and C253A mice supplemented with MitoQ. Remarkably, inflammatory pathways upregulated in C253A mice were completely renormalized upon MitoQ supplementation and additional inflammatory proteins were decreased (Figures 6E–6M and S6I–S6P; Table S5). Together, these data demonstrate a major role for UCP1 C253 in the regulation of inflammatory signaling in both subQ WAT and BAT following DIO that is dependent on mtROS. It should be noted, however, in agreement with previous literature (Fink et al., 2017; Rodriguez-Cuenca et al., 2010), mice supplemented with MitoQ in their drinking water gained less weight than control counterparts, which could additionally contribute to the above-described anti-inflammatory phenotypes observed.

Estrogen signaling underlies sex-dependent inflammation regulated by UCP1 C253

Next, to explore the mechanism by which UCP1 C253A female mice may be protected from inflammation we explored the role of estrogen signaling, which is known to confer systemic protective metabolic effects in the context of obesity (Dakin et al., 2015; Davis et al., 2013). We implanted slow release β-estradiol capsules subcutaneously in male WT and C253A mice prior to 12-week HFHS diet intervention (Figures S7A–S7D). The expression of inflammatory cytokines, which were significantly increased in BAT of untreated C253A mice, renormalized to WT levels upon β-estradiol supplementation (Figure 7A). Furthermore, the expression of the anti-inflammatory cytokine, *Il10*, which was decreased in BAT of UCP1 C253A mice, was also renormalized to WT levels. A similar phenotype was observed in subQ WAT (Figure 7B). Proteomic assessment of BAT and subQ WAT determined that many inflammatory proteins that were upregulated in UCP1 C253A mice were no longer significantly upregulated in C253A mice upon β-estradiol supplementation (Figures 7C–7K; Table S6) and several additional inflammatory proteins were downregulated (Figures S7E–S7L). A decrease in proteins associated with antigen processing and presentation (Figures S7I and S7J), phagocytosis (Figures S7I and S7K), and B cell signaling (Figures S7I and S7L), was observed in BAT from C253A mice following β-estradiol supplementation. Taken together, these data demonstrate that estrogen signaling plays a central role in antagonizing tis-

sue inflammation in BAT and subQ of mice lacking UCP1 C253. As previously reported (Martínez de Morentin et al., 2014), mice supplemented with β-estradiol gained less weight than control counterparts, which could additionally contribute to the anti-inflammatory phenotypes observed.

DISCUSSION

The recent identification of C253 as a residue that becomes covalently modified to elevate UCP1 activity has raised the question of the physiological importance of this regulatory site. More generally, it is now established that the widely used UCP1KO loss-of-function model is in fact depleted of the entire mitochondrial ETC, thus confounding the interpretation of many of the phenotypes and molecular functions assigned to UCP1. To address the physiological relevance of both UCP1 and C253 we generated the UCP1 C253A mouse. This model selectively abrogated regulatory activation of UCP1 by covalent modification of C253. Moreover, adipose tissues in UCP1 C253A mice exhibit no depletion of the mitochondrial ETC, and this is therefore a model for selective disruption of UCP1 *in vivo*. Mice lacking C253 of UCP1 exhibit a thermogenic deficit in response to the cold temperatures, demonstrating the importance of this residue in elevating UCP1 activity in response to thermal challenge. This finding is in line with previous work demonstrating the functional relevance of sulfenylation of C253 specifically upon exposure to cold temperatures (Chouchani et al., 2016; Shi et al., 2021). Interestingly, UCP1 C253A mice exhibited no decrease in energy expenditure or enhanced adiposity in an obesogenic environment. Absent a thermogenic stimulus that would elevate modification of UCP1 C253, such as exposure to cold temperatures, this site does not appear to play a role in energy expenditure or adiposity. This finding contrasts with data from the UCP1KO mouse, which exhibits elevated adiposity upon high-fat feeding, when housed at thermoneutral temperatures. Considering what is now known about depletion of the entire ETC in the UCP1KO model and our data herein, enhanced adiposity could be attributable to the combined depletion of the mitochondrial catabolic machinery, as opposed to UCP1 activity alone. Alternatively, activation of UCP1-dependent diet-induced thermogenesis by local increase of free fatty acids, independent of C253 modification, may explain this discrepancy. In addition, major UCP1-independent thermogenic processes are present in BAT that contribute to diet-induced thermogenesis, in particular the futile cycle of reversible creatine phosphorylation, for which there is now substantial genetic evidence (Kazak et al., 2015, 2017a, 2019; Rahbani et al., 2021; Sun et al., 2021). Our data suggest

---

(F) Protein abundance differences in subQ between male WT and UCP1 C253A supplemented with MitoQ following 12 weeks HFHS feeding. Top pathways enriched in proteins exhibiting >20% increase between WT and UCP1 C253A males in (E) are highlighted (WT n = 5; UCP1 C253A + MitoQ n = 6).

(G–J) Protein abundance differences of top enriched pathways (G–I) or established pro-inflammatory proteins from WT versus UCP1 C253A comparator (J) between WT and UCP1 C253A+MitoQ subQ following 12 weeks HFHS feeding (WT n = 5; UCP1 C253A+MitoQ n = 6).

(K) Protein abundance differences between WT and UCP1 C253A BAT following 12 weeks HFHS feeding with inflammatory proteins highlighted (n = 8). These data are additionally presented in Figure 4K.

(L) Protein abundance differences between WT and UCP1 C253A+MitoQ BAT following 12 weeks HFHS feeding with inflammatory proteins highlighted (WT n = 5; UCP1 C253A+MitoQ n = 6).

(M) Protein abundance differences of established pro-inflammatory proteins from WT versus UCP1 C253A comparator (K) between WT and UCP1 C253A+MitoQ BAT following 12 weeks HFHS feeding (WT n = 5; UCP1 C253A+MitoQ n = 6).

*p < 0.05, **p < 0.01 (two-tailed Student's t test for pairwise comparisons, one-way ANOVA for multiple comparisons involving independent variable). Data are mean ± SEM.
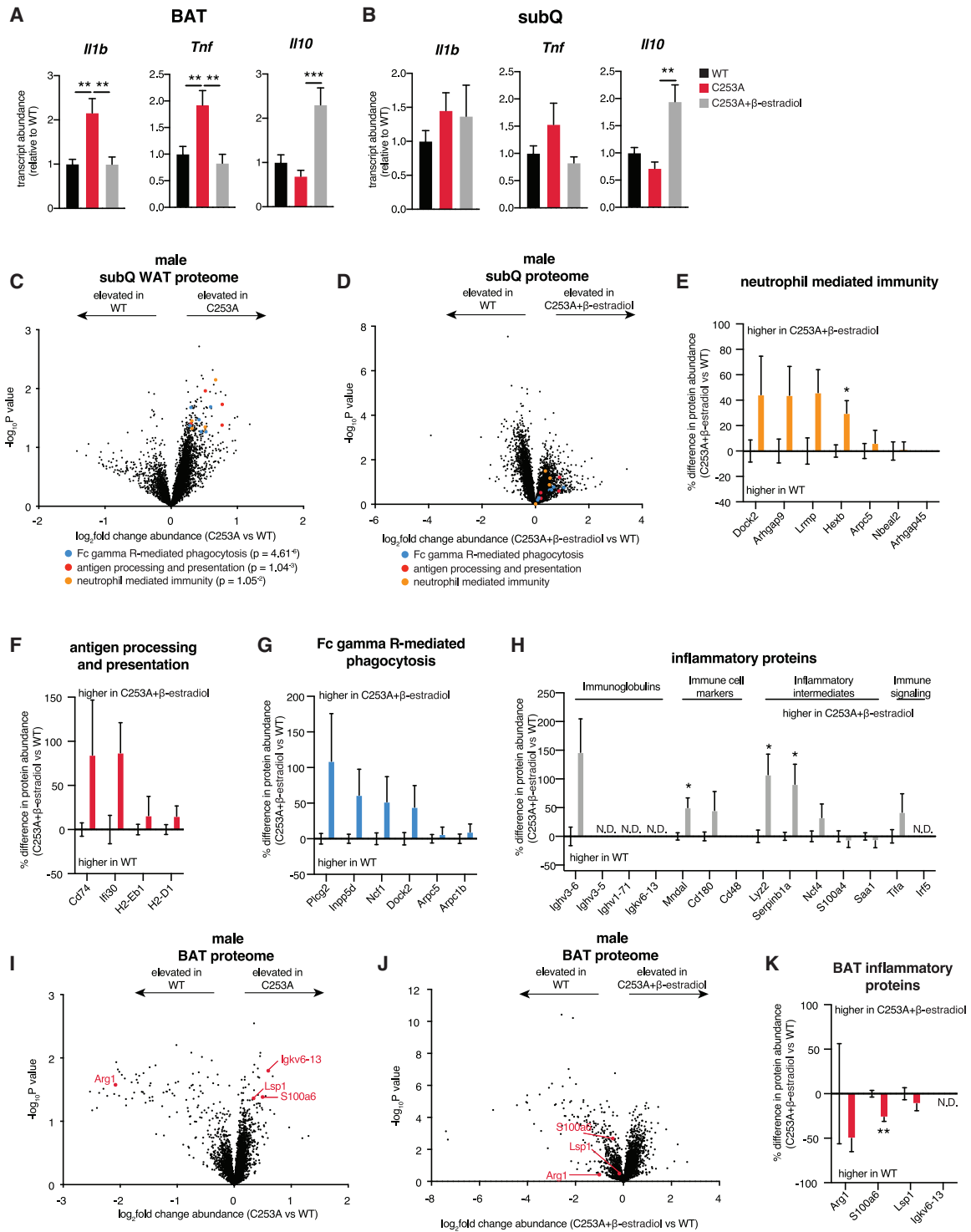
Figure 7. Estrogen signaling underlies sex-dependent inflammation regulated by UCP1 C253

(A) Relative gene expression of inflammatory intermediates in BAT from WT, UCP1 C253A, and UCP1 C253A mice supplemented with β-estradiol following 12 weeks on HFHS diet (WT n = 9; UCP1 C253A n = 9; UCP1 C253A + β-estradiol n = 10).

(B) Relative gene expression of inflammatory intermediates in subQ from WT, UCP1 C253A, and UCP1 C253A mice supplemented with β-estradiol following 12 weeks on HFHS diet (WT n = 8; UCP1 C253A n = 8–9; UCP1 C253A+β-estradiol n = 10–11).

(C) Protein abundance differences between male WT and UCP1 C253A subQ following 12 weeks HFHS feeding. Top pathways enriched in proteins exhibiting >20% increase between genotypes highlighted (WT n = 7; UCP1 C253A n = 5). These data are additionally presented in Figures 4A and 6E.

(legend continued on next page)

that these effector pathways play a greater role in diet-induced thermogenesis by BAT and beige fat.

The unexpected role for C253 of UCP1 in the regulation of white and BAT inflammation and glucose sensitivity suggests that, in the context of obesity, this site mediates adipose tissue inflammatory homeostasis. Moreover, the remarkable sex dependency of this effect reveals a previously unappreciated sexual dimorphism of UCP1 activity in the regulation of metabolic tissue inflammation. Based on our findings, the molecular basis for UCP1 C253 control over adipose tissue inflammation involves feedback control over redox homeostasis in BAT. We observe that in the absence of UCP1 C253, systematic alterations in mitochondrial macromolecular oxidation and damage occur in BAT, which are required to drive systemic pro-inflammatory signaling. These observations suggest that a major physiological role of UCP1 C253 is to maintain local redox homeostasis in BAT and beige fat, which produce significant levels of mitochondrial ROS due to their distinct catabolic capacities (Mills et al., 2018).

Our findings demonstrate that UCP1 C253 is necessary to antagonize major pathogenic inflammatory tissue remodeling in male mice in an obesogenic environment. The immune cell populations, cytokines, and pro-inflammatory molecules antagonized by UCP1 C253 are well established hallmarks of systemic metabolic pathologies such as T2D and insulin resistance in mice and humans (Engström et al., 2005; Fortuno et al., 2006; Kanda et al., 2006; Larsen et al., 2007; Liu et al., 2009; Lumeng et al., 2007; Maedler et al., 2002; Nishimura et al., 2009; Spranger et al., 2003; Xu et al., 2003; Yang et al., 2006). These include cytotoxic T cells and inflammatory macrophages, as well as the pro-inflammatory cytokines IL-1β and TNFand the chemokine CCL2. Our proteomics data further implicate a damaging inflammatory response in the adipose tissues of male C253A mice characterized by neutrophil-mediated immunity, activation of the NF-κB signaling pathway, and the production of DAMPs and acute phase proteins, all of which have been linked with glucose intolerance (Anguita-Ruiz et al., 2020; Arner et al., 2018; Eldor et al., 2006; Fortuno et al., 2006; Scheja et al., 2008; Wang et al., 2019; Yang et al., 2006). This pro-inflammatory remodeling of adipose tissue has been extensively linked with obesity-associated inflammation, pathology, and progression of T2D (Eldor et al., 2006; Lumeng et al., 2007; Maedler et al., 2002; Spranger et al., 2003). Indeed, we find that the UCP1 C253A inflammatory phenotype coincides with male-specific changes in glucose insensitivity. Finally, the sexually dimorphic nature of these findings supports what is known regarding the protection of pre-menopausal females from metabolic diseases such as T2D (Chella Krishnan et al., 2018; Davis et al., 2013) and positions UCP1 C253 as a regulator of this phenotype. It is well established that the incidence of T2D is lower in premenopausal, but not postmenopausal, women compared with men, and this is thought to be, in part, a consequence of decreased inflammation mediated via estrogen receptor signaling in females (Davis et al., 2013; Ghosh et al., 2019). Indeed, we show here that pharmacological elevation of estrogen signaling in males largely reverses inflammation driven by loss of UCP1 C253. In this light, our data demonstrate that UCP1 C253 is a critical regulator of acute thermogenic activation and systemic inflammatory homeostasis, with a specific role in protection from inflammatory metabolic pathogenesis in male mice. Moreover, we establish the UCP1 C253A mouse as an *in vivo* model for selective disruption of UCP1 activity.

Limitations of the study

We report, for the first time, a new mouse model to investigate the role of UCP1 in adipose tissue thermogenesis and systemic metabolism. The clear benefit of this new model is that, unlike UCP1KO mice, the BAT mitochondrial proteome of UCP1 C253A mice remains intact and thereby allows for a more precise delineation of the specific role of UCP1 in thermogenesis *in vivo*. However, although we see a clear thermogenic defect in these mice, it should be noted that this model may underrepresent the role of UCP1 as it specifically alters just one regulatory cysteine residue. We report that C253 of UCP1 regulates both local and systemic inflammation in a sex-dependent manner and that this correlates with male-specific glucose insensitivity. While this study and the literature strongly suggest that there is a causal link between these phenomena, we have not directly implicated this inflammatory phenotype as the fundamental driver of the observed glucose insensitivity. Furthermore, we did not elucidate the precise mechanism by which estrogen mediates its protective effects, an area that warrants further investigation given the profound sex dependency observed here and more generally in the realm of metabolic disease.

STAR★METHODS

Detailed methods are provided in the online version of this paper and include the following:

- KEY RESOURCES TABLE
- RESOURCE AVAILABILITY

(D) Protein abundance differences in subQ between male WT and UCP1 C253A supplemented with β-estradiol following 12 weeks HFHS feeding. Top pathways enriched in proteins exhibiting >20% increase between WT and UCP1 C253A males in (C) are highlighted (WT n = 5; UCP1 C253A+β-estradiol n = 6).

(E–H) Protein abundance differences of top enriched pathways (E–G) or established pro-inflammatory proteins (H) from WT versus UCP1 C253A comparator (C) between WT and UCP1 C253A+β-estradiol subQ following 12 weeks HFHS feeding as (WT n = 5; UCP1 C253A + β-estradriol n = 6).

(I) Protein abundance differences between WT and UCP1 C253A BAT following 12 weeks HFHS feeding with inflammatory proteins highlighted (n = 8). These data are additionally presented in Figures 4K and 6K.

(J) Protein abundance differences between WT and UCP1 C253A + β-estradiol BAT following 12 weeks HFHS feeding with inflammatory proteins highlighted (WT n = 5; UCP1 C253A + β-estradiol n = 6).

(K) Protein abundance differences of established pro-inflammatory proteins from WT versus UCP1 C253A comparator (I) between WT and UCP1 C253A+-β-estradiol BAT following 12 weeks HFHS feeding as (WT n = 5; UCP1 C253A+β-estradiol n = 6).

*p < 0.05, **p < 0.01, ***p < 0.001 (two-tailed Student's t test for pairwise comparisons, one-way ANOVA for multiple comparisons involving independent variable). Data are mean ± SEM.

AUTHOR CONTRIBUTIONS

E.L.M. designed research, carried out experiments, and analyzed data. H.X., M.P.J., J.S., and G.A.B. carried out and analyzed data from mass spectrometry experiments. R.G., D.L.-B., and N.T. assisted with animal physiology and imaging experiments. A.V.G. performed mtDNA experiments. C.H. and H.P. assisted with flow cytometry experiments. S.P.G. oversaw mass spectrometry experiments. L.L. oversaw flow cytometry experiments. M.P.M. oversaw mtDNA experiments. B.M.S. directed research. E.T.C. directed research and co-wrote the paper with assistance from the other authors.

REFERENCES

Aderem, A., and Underhill, D.M. (1999). Mechanisms of phagocytosis in macrophages. Annu. Rev. Immunol. 17, 593–623.

Anguita-Ruiz, A., Mendez-Gutierrez, A., Ruperez, A.I., Leis, R., Bueno, G., Gil-Campos, M., Tofe, I., Gomez-Llorente, C., Moreno, L.A., Gil, Á., and Aguilera, C.M. (2020). The protein S100A4 as a novel marker of insulin resistance in prepubertal and pubertal children with obesity. Metabolism 105, 154187.

Arner, P., Petrus, P., Esteve, D., Boulomié, A., Näslund, E., Thorell, A., Gao, H., Dahlman, I., and Rydén, M. (2018). Screening of potential adipokines identifies S100A4 as a marker of pernicious adipose tissue and insulin resistance. Int. J. Obes. (Lond) 42, 2047–2056.

Baskin, A.S., Linderman, J.D., Brychta, R.J., McGehee, S., Anflick-Chames, E., Cero, C., Johnson, J.W., O'Mara, A.E., Fletcher, L.A., Leitner, B.P., et al. (2018). Regulation of human adipose tissue activation, gallbladder size, and bile acid metabolism by a beta3-adrenergic receptor agonist. Diabetes 67, 2113–2125.

Becher, T., Palanisamy, S., Kramer, D.J., Eljalby, M., Marx, S.J., Wibmer, A.G., Butler, S.D., Jiang, C.S., Vaughan, R., Schöder, H., et al. (2021). Brown adipose tissue is associated with cardiometabolic health. Nat. Med. 27, 58–65.

Bloom, J.D., Dutia, M.D., Johnson, B.D., Wissner, A., Burns, M.G., Largis, E.E., Dolan, J.A., and Claus, T.H. (1992). Disodium (R,R)-5-[2-[[2-(3-chlorophenyl)-2-hydroxyethyl]-amino] propyl]-1,3-benzodioxole-2,2-dicarboxylate (CL 316,243). A potent beta-adrenergic agonist virtually specific for beta 3 receptors. A promising antidiabetic and antiobesity agent. J. Med. Chem. 35, 3081–3084.

Bordicchia, M., Liu, D., Amri, E.Z., Ailhaud, G., Dessì-Fulgheri, P., Zhang, C., Takahashi, N., Sarzani, R., and Collins, S. (2012). Cardiac natriuretic peptides act via p38 MAPK to induce the brown fat thermogenic program in mouse and human adipocytes. J. Clin. Invest. 122, 1022–1036.

Cani, P.D., Amar, J., Iglesias, M.A., Poggi, M., Knauf, C., Bastelica, D., Neyrinck, A.M., Fava, F., Tuohy, K.M., Chabo, C., et al. (2007). Metabolic endotoxemia initiates obesity and insulin resistance. Diabetes 56, 1761–1772.

Cannon, B., and Nedergaard, J. (2004). Brown adipose tissue: function and physiological significance. Physiol. Rev. 84, 277–359.

Chella Krishnan, K., Mehrabian, M., and Lusis, A.J. (2018). Sex differences in metabolism and cardiometabolic disorders. Curr. Opin. Lipidol. 29, 404–410.

Chen, E.Y., Tan, C.M., Kou, Y., Duan, Q., Wang, Z., Meirelles, G.V., Clark, N.R., and Ma'ayan, A. (2013a). Enrichr: interactive and collaborative HTML5 gene list enrichment analysis tool. BMC Bioinformatics 14, 128.

Chen, K.Y., Brychta, R.J., Linderman, J.D., Smith, S., Courville, A., Dieckmann, W., Herscovitch, P., Millo, C.M., Remaley, A., Lee, P., and Celi, F.S. (2013b). Brown fat activation mediates cold-induced thermogenesis in adult humans in response to a mild decrease in ambient temperature. J. Clin. Endocrinol. Metab. 98, E1218–E1223.

Chouchani, E.T., Kazak, L., Jedrychowski, M.P., Lu, G.Z., Erickson, B.K., Szpyt, J., Pierce, K.A., Laznik-Bogoslavski, D., Vetrivelan, R., Clish, C.B., et al. (2016). Mitochondrial ROS regulate thermogenic energy expenditure and sulfenylation of UCP1. Nature 532, 112–116.

Chouchani, E.T., Kazak, L., and Spiegelman, B.M. (2017). Mitochondrial reactive oxygen species and adipose tissue thermogenesis: bridging physiology and mechanisms. J. Biol. Chem. 292, 16810–16816.

Chouchani, E.T., Kazak, L., and Spiegelman, B.M. (2019). New advances in adaptive thermogenesis: UCP1 and beyond. Cell Metab 29, 27–37.

Collins, L.V., Hajizadeh, S., Holme, E., Jonsson, I.M., and Tarkowski, A. (2004). Endogenously oxidized mitochondrial DNA induces in vivo and in vitro inflammatory responses. J. Leukoc. Biol. *75*, 995–1000.

Crane, J.D., Mottillo, E.P., Farncombe, T.H., Morrison, K.M., and Steinberg, G.R. (2014). A standardized infrared imaging technique that specifically detects UCP1-mediated thermogenesis in vivo. Mol. Metab. *3*, 490–494.

Cypess, A.M., Lehman, S., Williams, G., Tal, I., Rodman, D., Goldfine, A.B., Kuo, F.C., Palmer, E.L., Tseng, Y.H., Doria, A., et al. (2009). Identification and importance of brown adipose tissue in adult humans. N. Engl. J. Med. *360*, 1509–1517.

Cypess, A.M., Weiner, L.S., Roberts-Toler, C., Franquet Elía, E., Kessler, S.H., Kahn, P.A., English, J., Chatman, K., Trauger, S.A., Doria, A., and Kolodny, G.M. (2015). Activation of human brown adipose tissue by a beta3-adrenergic receptor agonist. Cell Metab *21*, 33–38.

Dakin, R.S., Walker, B.R., Seckl, J.R., Hadoke, P.W., and Drake, A.J. (2015). Estrogens protect male mice from obesity complications and influence glucocorticoid metabolism. Int. J. Obes. (Lond) *39*, 1539–1547.

Davis, K.E., D Neinast, M., Sun, K., M Skiles, W., D Bills, J., A Zehr, J., Zeve, D., D Hahner, L., W Cox, D., Gent, L.M., et al. (2013). The sexually dimorphic role of adipose and adipocyte estrogen receptors in modulating adipose tissue expansion, inflammation, and fibrosis. Mol. Metab. *2*, 227–242.

Eldor, R., Yeffet, A., Baum, K., Doviner, V., Amar, D., Ben-Neriah, Y., Christofori, G., Peled, A., Carel, J.C., Boitard, C., et al. (2006). Conditional and specific NF-kappaB blockade protects pancreatic beta cells from diabetogenic agents. Proc. Natl. Acad. Sci. USA *103*, 5072–5077.

Elias, J.E., and Gygi, S.P. (2007). Target-decoy search strategy for increased confidence in large-scale protein identifications by mass spectrometry. Nat. Methods *4*, 207–214.

Enerbäck, S., Jacobsson, A., Simpson, E.M., Guerra, C., Yamashita, H., Harper, M.E., and Kozak, L.P. (1997). Mice lacking mitochondrial uncoupling protein are cold-sensitive but not obese. Nature *387*, 90–94.

Eng, J.K., Jahan, T.A., and Hoopmann, M.R. (2013). Comet: an open-source MS/MS sequence database search tool. Proteomics *13*, 22–24.

Eng, J.K., McCormack, A.L., and Yates, J.R. (1994). An approach to correlate tandem mass spectral data of peptides with amino acid sequences in a protein database. J. Am. Soc. Mass Spectrom. *5*, 976–989.

Engström, G., Hedblad, B., Eriksson, K.F., Janzon, L., and Lindgärde, F. (2005). Complement C3 is a risk factor for the development of diabetes: a population-based cohort study. Diabetes *54*, 570–575.

Feldmann, H.M., Golozoubova, V., Cannon, B., and Nedergaard, J. (2009). UCP1 ablation induces obesity and abolishes diet-induced thermogenesis in mice exempt from thermal stress by living at thermoneutrality. Cell Metab *9*, 203–209.

Fink, B.D., Guo, D.F., Kulkarni, C.A., Rahmouni, K., Kerns, R.J., and Sivitz, W.I. (2017). Metabolic effects of a mitochondrial-targeted coenzyme Q analog in high fat fed obese mice. Pharmacol. Res. Perspect. *5*, e00301.

Fleischman, A., Shoelson, S.E., Bernier, R., and Goldfine, A.B. (2008). Salsalate improves glycemia and inflammatory parameters in obese young adults. Diabetes Care *31*, 289–294.

Fortuno, A., San Jose, G., Moreno, M.U., Beloqui, O., Diez, J., and Zalba, G. (2006). Phagocytic NADPH oxidase overactivity underlies oxidative stress in metabolic syndrome. Diabetes *55*, 209–215.

Ghosh, S., Taylor, J.L., Mendoza, T.M., Dang, T., Burk, D.H., Yu, Y., Kilroy, G., and Floyd, Z.E. (2019). Siah2 modulates sex-dependent metabolic and inflammatory responses in adipose tissue to a high-fat diet challenge. Biol. Sex Differ. *10*, 19.

Goldfine, A.B., Fonseca, V., Jablonski, K.A., Pyle, L., Staten, M.A., and Shoelson, S.E.; TINSAL-T2D (Targeting Inflammation Using Salsalate in Type 2 Diabetes) Study Team (2010). The effects of salsalate on glycemic control in patients with type 2 diabetes: a randomized trial. Ann. Intern. Med. *152*, 346–357.

Goldfine, A.B., Silver, R., Aldhahi, W., Cai, D., Tatro, E., Lee, J., and Shoelson, S.E. (2008). Use of salsalate to target inflammation in the treatment of insulin resistance and type 2 diabetes. Clin. Transl. Sci. *1*, 36–43.

Goldgof, M., Xiao, C., Chanturiya, T., Jou, W., Gavrilova, O., and Reitman, M.L. (2014). The chemical uncoupler 2,4-dinitrophenol (DNP) protects against diet-induced obesity and improves energy homeostasis in mice at thermoneutrality. J. Biol. Chem. *289*, 19341–19350.

Granneman, J.G., Burnazi, M., Zhu, Z., and Schwamb, L.A. (2003). White adipose tissue contributes to UCP1-independent thermogenesis. Am. J. Physiol. Endocrinol. Metab. *285*, E1230–E1236.

Guo, J., and Hall, K.D. (2011). Predicting changes of body weight, body fat, energy expenditure and metabolic fuel selection in C57BL/6 mice. PLoS One *6*, e15961.

Han, Y.H., Buffolo, M., Pires, K.M., Pei, S., Scherer, P.E., and Boudina, S. (2016). Adipocyte-specific deletion of manganese superoxide dismutase protects from diet-induced obesity through increased mitochondrial uncoupling and biogenesis. Diabetes *65*, 2639–2651.

Himms-Hagen, J., Cui, J., Danforth, E., Jr., Taatjes, D.J., Lang, S.S., Waters, B.L., and Claus, T.H. (1994). Effect of CL-316,243, a thermogenic beta 3-agonist, on energy balance and brown and white adipose tissues in rats. Am. J. Physiol. *266*, R1371–R1382.

Hong, E.G., Ko, H.J., Cho, Y.R., Kim, H.J., Ma, Z., Yu, T.Y., Friedline, R.H., Kurt-Jones, E., Finberg, R., Fischer, M.A., et al. (2009). Interleukin-10 prevents diet-induced insulin resistance by attenuating macrophage and cytokine response in skeletal muscle. Diabetes *58*, 2525–2535.

Huttlin, E.L., Jedrychowski, M.P., Elias, J.E., Goswami, T., Rad, R., Beausoleil, S.A., Villén, J., Haas, W., Sowa, M.E., and Gygi, S.P. (2010). A tissue-specific atlas of mouse protein phosphorylation and expression. Cell *143*, 1174–1189.

Kamei, N., Tobe, K., Suzuki, R., Ohsugi, M., Watanabe, T., Kubota, N., Ohtsuka-Kowatari, N., Kumagai, K., Sakamoto, K., Kobayashi, M., et al. (2006). Overexpression of monocyte chemoattractant protein-1 in adipose tissues causes macrophage recruitment and insulin resistance. J. Biol. Chem. *281*, 26602–26614.

Kanda, H., Tateya, S., Tamori, Y., Kotani, K., Hiasa, K., Kitazawa, R., Kitazawa, S., Miyachi, H., Maeda, S., Egashira, K., and Kasuga, M. (2006). MCP-1 contributes to macrophage infiltration into adipose tissue, insulin resistance, and hepatic steatosis in obesity. J. Clin. Invest. *116*, 1494–1505.

Kazak, L., Chouchani, E.T., Jedrychowski, M.P., Erickson, B.K., Shinoda, K., Cohen, P., Vetrivelan, R., Lu, G.Z., Laznik-Bogoslavski, D., Hasenfuss, S.C., et al. (2015). A creatine-driven substrate cycle enhances energy expenditure and thermogenesis in beige fat. Cell *163*, 643–655.

Kazak, L., Chouchani, E.T., Lu, G.Z., Jedrychowski, M.P., Bare, C.J., Mina, A.I., Kumari, M., Zhang, S., Vuckovic, I., Laznik-Bogoslavski, D., et al. (2017a). Genetic depletion of adipocyte creatine metabolism inhibits diet-induced thermogenesis and drives obesity. Cell Metab *26*, 660–671.e3.

Kazak, L., Chouchani, E.T., Stavrovskaya, I.G., Lu, G.Z., Jedrychowski, M.P., Egan, D.F., Kumari, M., Kong, X., Erickson, B.K., Szpyt, J., et al. (2017b). UCP1 deficiency causes brown fat respiratory chain depletion and sensitizes mitochondria to calcium overload-induced dysfunction. Proc. Natl. Acad. Sci. USA *114*, 7981–7986.

Kazak, L., Rahbani, J.F., Samborska, B., Lu, G.Z., Jedrychowski, M.P., Lajoie, M., Zhang, S., Ramsay, L.C., Dou, F.Y., Tenen, D., et al. (2019). Ablation of adipocyte creatine transport impairs thermogenesis and causes diet-induced obesity. Nat. Metab. *1*, 360–370.

Kir, S., White, J.P., Kleiner, S., Kazak, L., Cohen, P., Baracos, V.E., and Spiegelman, B.M. (2014). Tumour-derived PTH-related protein triggers adipose tissue browning and cancer cachexia. Nature *513*, 100–104.

Koska, J., Ortega, E., Bunt, J.C., Gasser, A., Impson, J., Hanson, R.L., Forbes, J., de Courten, B., and Krakoff, J. (2009). The effect of salsalate on insulin action and glucose tolerance in obese non-diabetic patients: results of a randomised double-blind placebo-controlled study. Diabetologia *52*, 385–393.

Kuleshov, M.V., Jones, M.R., Rouillard, A.D., Fernandez, N.F., Duan, Q., Wang, Z., Koplev, S., Jenkins, S.L., Jagodnik, K.M., Lachmann, A., et al. (2016). Enrichr: a comprehensive gene set enrichment analysis web server 2016 update. Nucleic Acids Res *44*, W90–W97.

Lafontan, M., and Berlan, M. (1993). Fat cell adrenergic receptors and the control of white and brown fat cell function. J. Lipid Res. *34*, 1057–1091.

Larsen, C.M., Faulenbach, M., Vaag, A., Ehses, J.A., Donath, M.Y., and Mandrup-Poulsen, T. (2009). Sustained effects of interleukin-1 receptor antagonist treatment in type 2 diabetes. Diabetes Care 32, 1663–1668.

Larsen, C.M., Faulenbach, M., Vaag, A., Vølund, A., Ehses, J.A., Seifert, B., Mandrup-Poulsen, T., and Donath, M.Y. (2007). Interleukin-1-receptor antagonist in type 2 diabetes mellitus. N. Engl. J. Med. 356, 1517–1526.

Lee, S.J., Kim, S.H., Park, K.M., Lee, J.H., and Park, J.W. (2016). Increased obesity resistance and insulin sensitivity in mice lacking the isocitrate dehydrogenase 2 gene. Free Radic. Biol. Med. 99, 179–188.

Lettieri Barbato, D., Tatulli, G., Maria Cannata, S., Bernardini, S., Aquilano, K., and Ciriolo, M.R. (2015). Glutathione decrement drives thermogenic program in adipose cells. Sci. Rep. 5, 13091.

Lim, J., Iyer, A., Suen, J.Y., Seow, V., Reid, R.C., Brown, L., and Fairlie, D.P. (2013). C5aR and C3aR antagonists each inhibit diet-induced obesity, metabolic dysfunction, and adipocyte and macrophage signaling. FASEB J 27, 822–831.

Liu, D., Bordicchia, M., Zhang, C., Fang, H., Wei, W., Li, J.L., Guilherme, A., Guntur, K., Czech, M.P., and Collins, S. (2016). Activation of mTORC1 is essential for beta-adrenergic stimulation of adipose browning. J. Clin. Invest. 126, 1704–1716.

Liu, J., Divoux, A., Sun, J., Zhang, J., Clément, K., Glickman, J.N., Sukhova, G.K., Wolters, P.J., Du, J., Gorgun, C.Z., et al. (2009). Genetic deficiency and pharmacological stabilization of mast cells reduce diet-induced obesity and diabetes in mice. Nat. Med. 15, 940–945.

Lowell, B.B., S-Susulic, V., Hamann, A., Lawitts, J.A., Himms-Hagen, J., Boyer, B.B., Kozak, L.P., and Flier, J.S. (1993). Development of obesity in transgenic mice after genetic ablation of brown adipose tissue. Nature 366, 740–742.

Lumeng, C.N., Bodzin, J.L., and Saltiel, A.R. (2007). Obesity induces a phenotypic switch in adipose tissue macrophage polarization. J. Clin. Invest. 117, 175–184.

Maedler, K., Sergeev, P., Ris, F., Oberholzer, J., Joller-Jemelka, H.I., Spinas, G.A., Kaiser, N., Halban, P.A., and Donath, M.Y. (2002). Glucose-induced beta cell production of IL-1beta contributes to glucotoxicity in human pancreatic islets. J. Clin. Invest. 110, 851–860.

Martínez de Morentin, P.B., González-García, I., Martins, L., Lage, R., Fernández-Mallo, D., Martínez-Sánchez, N., Ruíz-Pino, F., Liu, J., Morgan, D.A., Pinilla, L., et al. (2014). Estradiol regulates brown adipose tissue thermogenesis via hypothalamic AMPK. Cell Metab 20, 41–53.

McAlister, G.C., Nusinow, D.P., Jedrychowski, M.P., Wühr, M., Huttlin, E.L., Erickson, B.K., Rad, R., Haas, W., and Gygi, S.P. (2014). MultiNotch MS3 enables accurate, sensitive, and multiplexed detection of differential expression across cancer cell line proteomes. Anal. Chem. 86, 7150–7158.

Mills, E.L., Harmon, C., Jedrychowski, M.P., Xiao, H., Garrity, R., Tran, N.V., Bradshaw, G.A., Fu, A., Szpyt, J., Reddy, A., et al. (2021). UCP1 governs liver extracellular succinate and inflammatory pathogenesis. Nat. Metab. 3, 604–617.

Mills, E.L., Pierce, K.A., Jedrychowski, M.P., Garrity, R., Winther, S., Vidoni, S., Yoneshiro, T., Spinelli, J.B., Lu, G.Z., Kazak, L., et al. (2018). Accumulation of succinate controls activation of adipose tissue thermogenesis. Nature 560, 102–106.

Mócsai, A. (2013). Diverse novel functions of neutrophils in immunity, inflammation, and beyond. J. Exp. Med. 210, 1283–1299.

Muzik, O., Mangner, T.J., Leonard, W.R., Kumar, A., and Granneman, J.G. (2017). Sympathetic innervation of cold-activated brown and white fat in lean young adults. J. Nucl. Med. 58, 799–806.

Navarrete-Perea, J., Yu, Q., Gygi, S.P., and Paulo, J.A. (2018). Streamlined tandem mass tag (SL-TMT) protocol: an efficient strategy for quantitative (phospho)proteome profiling using tandem mass tag-synchronous precursor selection-MS3. J. Proteome Res. 17, 2226–2236.

Nishimura, S., Manabe, I., Nagasaki, M., Eto, K., Yamashita, H., Ohsugi, M., Otsu, M., Hara, K., Ueki, K., Sugiura, S., et al. (2009). CD8+ effector T cells contribute to macrophage recruitment and adipose tissue inflammation in obesity. Nat. Med. 15, 914–920.

Oka, T., Hikoso, S., Yamaguchi, O., Taneike, M., Takeda, T., Tamai, T., Oyabu, J., Murakawa, T., Nakayama, H., Nishida, K., et al. (2012). Mitochondrial DNA that escapes from autophagy causes inflammation and heart failure. Nature 485, 251–255.

Okada, K., LeClair, K.B., Zhang, Y., Li, Y., Ozdemir, C., Krisko, T.I., Hagen, S.J., Betensky, R.A., Banks, A.S., and Cohen, D.E. (2016). Thioesterase superfamily member 1 suppresses cold thermogenesis by limiting the oxidation of lipid droplet-derived fatty acids in brown adipose tissue. Mol. Metab. 5, 340–351.

Orava, J., Nuutila, P., Lidell, M.E., Oikonen, V., Noponen, T., Viljanen, T., Scheinin, M., Taittonen, M., Niemi, T., Enerbäck, S., and Virtanen, K.A. (2011). Different metabolic responses of human brown adipose tissue to activation by cold and insulin. Cell Metab 14, 272–279.

Ouellet, V., Labbé, S.M., Blondin, D.P., Phoenix, S., Guérin, B., Haman, F., Turcotte, E.E., Richard, D., and Carpentier, A.C. (2012). Brown adipose tissue oxidative metabolism contributes to energy expenditure during acute cold exposure in humans. J. Clin. Invest. 122, 545–552.

Peng, J., Elias, J.E., Thoreen, C.C., Licklider, L.J., and Gygi, S.P. (2003). Evaluation of multidimensional chromatography coupled with tandem mass spectrometry (LC/LC-MS/MS) for large-scale protein analysis: the yeast proteome. J. Proteome Res. 2, 43–50.

Rahbani, J.F., Roesler, A., Hussain, M.F., Samborska, B., Dykstra, C.B., Tsai, L., Jedrychowski, M.P., Vergnes, L., Reue, K., Spiegelman, B.M., and Kazak, L. (2021). Creatine kinase B controls futile creatine cycling in thermogenic fat. Nature 590, 480–485.

Ravussin, Y., Gutman, R., LeDuc, C.A., and Leibel, R.L. (2013). Estimating energy expenditure in mice using an energy balance technique. Int. J. Obes. (Lond) 37, 399–403.

Ro, S.H., Nam, M., Jang, I., Park, H.W., Park, H., Semple, I.A., Kim, M., Kim, J.S., Park, H., Einat, P., et al. (2014). Sestrin2 inhibits uncoupling protein 1 expression through suppressing reactive oxygen species. Proc. Natl. Acad. Sci. USA 111, 7849–7854.

Rodriguez-Cuenca, S., Cochemé, H.M., Logan, A., Abakumova, I., Prime, T.A., Rose, C., Vidal-Puig, A., Smith, A.C., Rubinsztein, D.C., Fearnley, I.M., et al. (2010). Consequences of long-term oral administration of the mitochondria-targeted antioxidant MitoQ to wild-type mice. Free Radic. Biol. Med. 48, 161–172.

Sanchez-Alavez, M., Bortell, N., Galmozzi, A., Conti, B., and Marcondes, M.C. (2014). Reactive oxygen species scavenger N-acetyl cysteine reduces methamphetamine-induced hyperthermia without affecting motor activity in mice. Temperature (Austin) 1, 227–241.

Sanchez-Alavez, M., Conti, B., Wood, M.R., Bortell, N., Bustamante, E., Saez, E., Fox, H.S., and Marcondes, M.C. (2013). ROS and sympathetically mediated mitochondria activation in brown adipose tissue contribute to methamphetamine-induced hyperthermia. Front. Endocrinol. 4, 44.

Scheja, L., Heese, B., Zitzer, H., Michael, M.D., Siesky, A.M., Pospisil, H., Beisiegel, U., and Seedorf, K. (2008). Acute-phase serum amyloid A as a marker of insulin resistance in mice. Exp. Diabetes Res. 2008, 230837.

Schneider, K., Valdez, J., Nguyen, J., Vawter, M., Galke, B., Kurtz, T.W., and Chan, J.Y. (2016). Increased energy expenditure, Ucp1 expression, and resistance to diet-induced obesity in mice lacking nuclear factor-erythroid-2-related transcription factor-2 (Nrf2). J. Biol. Chem. 291, 7754–7766.

Schweppe, D.K., Eng, J.K., Yu, Q., Bailey, D., Rad, R., Navarrete-Perea, J., Huttlin, E.L., Erickson, B.K., Paulo, J.A., and Gygi, S.P. (2020). Full-featured, real-time database searching platform enables fast and accurate multiplexed quantitative proteomics. J. Proteome Res. 19, 2026–2034.

Schweppe, D.K., Prasad, S., Belford, M.W., Navarrete-Perea, J., Bailey, D.J., Huguet, R., Jedrychowski, M.P., Rad, R., McAlister, G., Abbatiello, S.E., et al. (2019). Characterization and optimization of multiplexed quantitative analyses using high-field asymmetric-waveform ion mobility mass spectrometry. Anal. Chem. 91, 4010–4016.

Shapira, S.N., and Seale, P. (2019). Transcriptional control of brown and beige fat development and function. Obesity (Silver Spring) 27, 13–21.

Shi, M., Huang, X.-Y., Ren, X.-Y., Wei, X.Y., Ma, Y., Lin, Z.-Z., Liu, D.-T., Song, L., Zhao, T.-J., Li, G., et al. (2021). AIDA directly connects sympathetic innervation to adaptive thermogenesis by UCP1. Nat. Cell Biol. *23*, 268–277.

Shimada, K., Crother, T.R., Karlin, J., Dagvadorj, J., Chiba, N., Chen, S., Ramanujan, V.K., Wolf, A.J., Vergnes, L., Ojcius, D.M., et al. (2012). Oxidized mitochondrial DNA activates the NLRP3 inflammasome during apoptosis. Immunity *36*, 401–414.

Spranger, J., Kroke, A., Möhlig, M., Hoffmann, K., Bergmann, M.M., Ristow, M., Boeing, H., and Pfeiffer, A.F. (2003). Inflammatory cytokines and the risk to develop type 2 diabetes: results of the prospective population-based European Prospective Investigation into Cancer and Nutrition (EPIC)-Potsdam Study. Diabetes *52*, 812–817.

Sun, K., Tordjman, J., Clément, K., and Scherer, P.E. (2013). Fibrosis and adipose tissue dysfunction. Cell Metab *18*, 470–477.

Sun, Y., Rahbani, J.F., Jedrychowski, M.P., Riley, C.L., Vidoni, S., Bogoslavski, D., Hu, B., Dumesic, P.A., Zeng, X., Wang, A.B., et al. (2021). Mitochondrial TNAP controls thermogenesis by hydrolysis of phosphocreatine. Nature *593*, 580–585.

Talukdar, S., Oh, D.Y., Bandyopadhyay, G., Li, D., Xu, J., McNelis, J., Lu, M., Li, P., Yan, Q., Zhu, Y., et al. (2012). Neutrophils mediate insulin resistance in mice fed a high-fat diet through secreted elastase. Nat. Med. *18*, 1407–1412.

Ukropec, J., Anunciado, R.P., Ravussin, Y., Hulver, M.W., and Kozak, L.P. (2006). UCP1-independent thermogenesis in white adipose tissue of cold-acclimated Ucp1-/- mice. J. Biol. Chem. *281*, 31894–31908.

van Marken Lichtenbelt, W.D., Vanhommerig, J.W., Smulders, N.M., Drossaerts, J.M., Kemerink, G.J., Bouvy, N.D., Schrauwen, P., and Teule, G.J. (2009). Cold-activated brown adipose tissue in healthy men. N. Engl. J. Med. *360*, 1500–1508.

Virtanen, K.A., Lidell, M.E., Orava, J., Heglind, M., Westergren, R., Niemi, T., Taittonen, M., Laine, J., Savisto, N.J., Enerbäck, S., and Nuutila, P. (2009). Functional brown adipose tissue in healthy adults. N. Engl. J. Med. *360*, 1518–1525.

Wang, Y., Cao, F., Wang, Y., Yu, G., and Jia, B.L. (2019). Silencing of SAA1 inhibits palmitate- or high-fat diet induced insulin resistance through suppression of the NF-kappaB pathway. Mol. Med. *25*, 17.

Wlazlo, N., van Greevenbroek, M.M., Ferreira, I., Feskens, E.J., van der Kallen, C.J., Schalkwijk, C.G., Bravenboer, B., and Stehouwer, C.D. (2014). Complement factor 3 is associated with insulin resistance and with incident type 2 diabetes over a 7-year follow-up period: the CODAM Study. Diabetes Care *37*, 1900–1909.

Xiao, H., Jedrychowski, M.P., Schweppe, D.K., Huttlin, E.L., Yu, Q., Heppner, D.E., Li, J., Long, J., Mills, E.L., Szpyt, J., et al. (2020). A quantitative tissue-specific landscape of protein redox regulation during. Aging Cell *180*, 968–983, e924.

Xie, Z., Bailey, A., Clarke, D.J.B., Kuleshov, M.V., Evangenlista, J.E., Jenkins, S.L., Lachmann, A., Wojciechowicz, M.L., Kropiwnicki, E., Ma'ayan, A., Jagodnik, K.M., and Jeon, M. (2021). Gene set knowledge discovery with Enrichr. Current Protocols *1*, e90.

Xu, H., Barnes, G.T., Yang, Q., Tan, G., Yang, D., Chou, C.J., Sole, J., Nichols, A., Ross, J.S., Tartaglia, L.A., and Chen, H. (2003). Chronic inflammation in fat plays a crucial role in the development of obesity-related insulin resistance. J. Clin. Invest. *112*, 1821–1830.

Yang, R.Z., Lee, M.J., Hu, H., Pollin, T.I., Ryan, A.S., Nicklas, B.J., Snitker, S., Horenstein, R.B., Hull, K., Goldberg, N.H., et al. (2006). Acute-phase serum amyloid A: an inflammatory adipokine and potential link between obesity and its metabolic complications. PLoS Med *3*, e287.

Zewinger, S., Reiser, J., Jankowski, V., Alansary, D., Hahm, E., Triem, S., Klug, M., Schunk, S.J., Schmit, D., Kramann, R., et al. (2020). Apolipoprotein C3 induces inflammation and organ damage by alternative inflammasome activation. Nat. Immunol. *21*, 30–41.

Zhang, Q., Raoof, M., Chen, Y., Sumi, Y., Sursal, T., Junger, W., Brohi, K., Itagaki, K., and Hauser, C.J. (2010). Circulating mitochondrial DAMPs cause inflammatory responses to injury. Nature *464*, 104–107.

STAR★METHODS

KEY RESOURCES TABLE

REAGENT or RESOURCE	SOURCE	IDENTIFIER
Antibodies		
UCP1	Abcam	Cat#AB10983; RRID:AB_2241462
total OXPHOS	Abcam	Cat#AB110413; RRID:AB_2629281
Vinculin	Sigma	Cat#V9264; RRID:AB_10603627
beta-actin	Cell Signalling Technology	Cat#3700S; RRID:AB_2242334
Anti-Mouse IgG HRP Conjugate	Promega	Cat#W4021; RRID:AB_430834
Anti-Rabbit IgG HRP Conjugate	Promega	Cat#W4011; RRID:AB_430833
CD4 (FITC; GK1.5)	Biolegend	Cat#100406; RRID:AB_312691
CD19 (PerCP-Cy5.5; 6D5)	Biolegend	Cat#115534; RRID:AB_2072925
F4/80 (PE-CY7; BM8)	Biolegend	Cat#123114; RRID:AB_893478)
CD8a (APC/CY7; 53-6.7)	Biolegend	Cat#100713; RRID:AB_312752
CD11b (EF450; M1/70)	eBioscience	Cat#48-0112-82; RRID:AB_1582236
CD3 (BV412; 17A2)	Biolegend	Cat#100227; RRID:AB_10900227
CD3 (BV605; 17A2)	Biolegend	Cat#100237; RRID:AB_2562039
CD11c (BV711; N418)	Biolegend	Cat#117349; RRID:AB_2563905
CD45 (BV785; 30-F11)	Biolegend	Cat#103149; RRID:AB_2564590
Fc-receptor-blocking antibody	eBioscience	Cat#14-0161-82; RRID:AB_467133
Chemicals, peptides, and recombinant proteins		
Cysteine-reactive phosphate tags (CPTs)	Synthesized in house	N/A
10-plex TMT reagents	ThermoFisher Scientific	Cat#90406
16-plex TMT reagents	Thermo Fisher Scientific	Cat#A44520
2,4-Dinitrophenol	MilliporeSigma	Cat#D198501
3,3',5-Triiodo-L-thyronine (T3)	Sigma-Aldrich	Cat#T2877
4X NuPAGE LDS sample buffer	Thermo Fisher Scientific	Cat#NP0007
90-day release 17-β estradiol pellets	Innovation research of America	Cat#NE-121
Acetonitrile	Fisher Scientific	Cat# A9964
Ammonium acetate	Sigma	Cat#372331-100G
Ammonium hydroxide	Sigma	Cat# 338818-100ML
Antimycin	Sigma	Cat#A8674
Beta-mercaptoethanol	Sigma	Cat#M6250
Bond-Breaker TCEP Solution, Neutral pH	ThermoFisher Scientific	Cat#77720
Bovine Serum Albumin	Sigma	Cat#A9647
Collagenase B	Sigma-Aldrich	Cat#COLLB-RO
collagenase type II	Worthington	Cat#LS0041771
cOmplete Protease Inhibitor Cocktail	Sigma-Aldrich	Cat#CO-RO
D-glucose-13C6	Cambridge Isotope	Cat#CLM-1396-PK
Dexamethasone	Sigma-Aldrich	Cat#D4902
Dithiothreitol (DTT)	Sigma-Aldrich	Cat#DTT-RO
DMEM/F-12, GlutaMAX	Life Technologies	Cat#10565042
DMEM/F-12+Glutamax	Invitrogen	Cat#10565-042
EPPS	Sigma-Aldrich	Cat#E9502
fatty acid free BSA	Sigma-Aldrich	Cat#A6003
Fetal Bovine Serum	Gemini Bio-Products	Cat#100-106
Fixation buffer	Biolegend	Cat#420801
Formalin, Buffered, 10%	Fisher Scientific	Cat#SF100-4

(Continued on next page)

Continued

REAGENT or RESOURCE	SOURCE	IDENTIFIER
Glycocholate-d4	Cambridge Isotope	Cat#DLM-2742
GoTaq qPCR master mix	Promega	Cat#A6001
Indomethacin	Sigma-Aldrich	Cat#I7378
Inosine-15N4	Cambridge Isotope	Cat#NLM-4264
Insulin	Sigma-Aldrich	Cat#I5500
Iodoacetamide	Sigma-Aldrich	Cat#I1149
Isobutylmethylxanthine(IBMX)	Sigma-Aldrich	Cat#I7018
Lambda phosphatase	Santa Cruz Biotechnology	Cat#sc-200312
Lys-C	Wako Chemicals	Cat#125-05061
Methanol	Fisher Scientific	Cat# A4124
MitoQ	Mike Murphy	gifted
Norepinephrine	Sigma-Aldrich	Cat#A9512
oligomycin	MilliporeSigma	Cat#80058-538
Penicillin streptomycin	Fisher scientific	Cat#15-140-163
Pierce ECL Western Blotting Substrate	Life Technologies	Cat#32106
Rosiglitazone	Cayman	Cat#71740
Rotenone	Sigma-Aldrich	Cat#R8875
RPMI	Life Technologies	Cat#21870-076
Thymine-d4	Cambridge Isotope	Cat#DLM-1089
Trizol	Life Technologies	Cat#15596026
Trypan Blue	Sigma	Cat#T8154
Trypsin	Promega	Cat#V5113
Tween-20	Sigma	Cat#P9416
Zombie Aqua Live/dead stain	Biolegend	Cat#423101
ddPCR Supermix	Bio-rad	Cat#186-3024
DNeasy Blood & Tissue Kit	Qiagen	Cat #69504
Critical commercial assays		
High-Select Fe-NTA Phosphopeptide Enrichment Kit	ThermoFisher Scientific	Cat#A32992
Pierce High pH Reversed-Phase Peptide Fractionation Kit	ThermoFisher Scientific	Cat#84868
Micro BCA™ Protein Assay Kit	ThermoFisher Scientific	Cat#23235
RNA Mini Kit	Invitrogen	Cat#12183025
High-capacity cDNA reverse transcription kit	Fisher Scientific	Cat# 4368813
PureLink RNA Mini Kit	Life Technologies	Cat#12183025
Deposited data		
Deposited proteomics data	PRIDE	PXD029270
Experimental models: Organisms/strains		
C253A mice	This paper	N/A
Oligonucleotides		
See Table S7		N/A
Software and algorithms		
Xcalibur	ThermoFisher Scientific	Cat#OPTON-30965
TraceFinder	ThermoFisher Scientific	Cat#OPTON-30688
Adipocount		https://www.ncbi.nlm.nih.gov/pmc/articles/PMC5826178/
Adiposoft plugin		https://imagej.net/plugins/adiposoft
AMIDE medical imaging software		http://amide.sourceforge.net/
Biorender		https://biorender.com/

(Continued on next page)

Continued

REAGENT or RESOURCE	SOURCE	IDENTIFIER
Enrichr	Chen et al., 2013b; Kuleshov et al., 2016; Xie et al., 2021	https://amp.pharm.mssm.edu/Enrichr/
FACSDiva software	BD Biosciences	N/A
FLIR Tools software	https://support.flir.com/SwDownload/app/RssSWDownload.aspx?ID=1247	FLIR Tools software
FlowJo v10 software	Tree Star	N/A
ImageJ	NIH	https://imagej.nih.gov/ij/
In-house mass spectrometry data analysis software	Huttlin et al., 2010	N/A
NIS-Elements software	Nikon	N/A
Prism 8	GraphPad	https://www.graphpad.com/scientific-software/prism/
SEQUEST	Eng et al., 1994	https://doi.org/10.1016/1044-0305(94)80016-2
BIORAD QuantaSoft software	Bio-rad	Cat#1864011
Other		
Q-Exactive HF-X mass spectrometer	ThermoFisher Scientific	Cat#0726042
Quant Studio 6 Flex Real-Time PCR machine	Applied Biosciences	Cat# 44-856-99
UltiMate 3000 HPLC	ThermoFisher Scientific	IQLAAAGABHFAPBMBFC
Seahorse XF24 Extracellular Flux Analyzer	Agilent	N/A
Sep-Pak C18 Cartridges	Waters	Cat#WAT054955
SunFire Prep C18 5 μm OBD column	Waters	Cat#186003969
TCC-3000RS Thermostatted Column Compartment	ThermoFisher Scientific	Cat#5730.0000
TissueLyser II	QIAGEN	Cat#85300
Ultrasound machine	Philips	Affiniti70
WPS-3000TBFC Biocompatible Well Plate Autosampler	ThermoFisher Scientific	Cat#5841.0020
XF24 V7 cell culture microplates	Agilent	Cat#100777-004
2489 UV/Visible Detector	Waters	Cat#2489
2545 Binary Gradient Module	Waters	Cat#2545
Count beads	Spherotech	Cat#ACFD-50-5
EASY-nLC 1200 System	ThermoFisher Scientific	Cat#LC140
EchoMRI (model ET-025)	Echo Medical Systems	N/A
FAIMSPro	ThermoFisher Scientific	Cat#FMS02-10001
FLIR thermal imaging camera (Model FLIR-T62101).	FLIR	model discontinued
Glucometer, ultra mini	One Touch	N/A
Heparin columns	Becton Dickinson	Cat# 365985
High-fat diet	OpenSource Diets	Cat#D12492
High-fat high-sucrose diet	OpenSource Diets	Cat#D09071702
Agilent technologies 1200 series HPLC	Agilent	N/A
LPG-3400RS Quaternary Pump w/ Degasser	ThermoFisher Scientific	Cat#5040.0036
LSRFortessa	BD Biosciences	
Luna 5 μm NH2 column	Phenomenex	Cat#00F-4378-B0
MilliporeSigma™ Immobilon™-P PVDF Transfer Membranes	MilliporeSigma	Cat#IPVH00010
Multi-Therm heat-shake	Sigma-Aldrich	Cat#Z755753
Nanodrop 2000	Thermo Fisher	Cat#ND-2000
1260 Infinity II LC System	Agilent	N/A

Continued

REAGENT or RESOURCE	SOURCE	IDENTIFIER
NuPAGE™ 4 to 12%, Bis-Tris, 1.5 mm, Mini Protein Gel, 15-well	Thermo Fisher Scientific	Cat#NP0336BOX
Orbitrap Eclipse mass spectrometer	ThermoFisher Scientific	Cat#FSN04-10000
Orbitrap Fusion Lumos Mass Spectrometer	ThermoFisher Scientific	Cat#IQLAAEGAAPFADBMBHQ
BIORAD C1000 Thermo Cycler	Bio-rad	Cat#1851197
BIORAD ddPCR AutoDG	Bio-rad	Cat#1864101
BIORAD QX200 Droplet Reader	Bio-rad	Cat#1864003

RESOURCE AVAILABILITY

Lead contact
Edward Chouchani (EdwardT_Chouchani@dfci.harvard.edu).

Materials availability
Materials and data generated from this study is available upon request from Edward Chouchani (EdwardT_Chouchani@dfci.harvard.edu).

Data and code availability
Proteomics data have been deposited at PRIDE and are publicly available as of the date of publication. Accession numbers are listed in the key resources table. This paper does not report original code. Any additional information required to reanalyze the data reported in this paper is available from the lead contact upon request.

EXPERIMENTAL MODEL AND SUBJECT DETAILS

Mouse lines
Animal experiments were performed according to procedures approved by the Institutional Animal Care and Use Committee of the Beth Israel Deaconess Medical Center. Unless otherwise stated, mice used were male and female C57BL/6J (8–12 weeks of age; Jackson Laboratories) and housed in a temperature-controlled (22°C) room on a 12 h light/dark cycle.

Stromal vascular fraction (SVF) cell preparation from BAT and differentiation *in vitro*
Interscapular brown adipose stromal vascular fraction was obtained from 2- to 6-day-old male and female pups as described previously (Kir et al., 2014). Interscapular brown adipose was dissected, washed in PBS, minced, and digested for 45 min at 37 °C in PBS containing 1.5 mg ml^{-1} collagenase B, 123 mM NaCl, 5 mM KCl, 1.3 mM CaCl$_2$, 5 mM glucose, 100 mM HEPES, and 4% essentially fatty-acid-free BSA. Tissue suspension was filtered through a 40 μm cell strainer and centrifuged at 600g for 5 min to pellet the SVF. The cell pellet was resuspended in adipocyte culture medium and plated. Cells were maintained at 37°C in 10% CO$_2$. Primary brown pre-adipocytes were counted and plated in the evening, 12 h before differentiation at 150,000 cells/ml. Pre-adipocyte plating was scaled according to surface area. The following morning, brown pre-adipocytes were induced to differentiate for 2 days with an adipogenic cocktail (1 μM rosiglitazone, 0.5 mM IBMX, 5 μM dexamethasone, 0.114 μg ml−1 insulin, 1 nM T3, and 125 μM Indomethacin) in adipocyte culture medium. Two days after induction, cells were re-fed every 48 h with adipocyte culture medium containing 1 μM rosiglitazone and 0.5 μg ml^{-1} insulin. Cells were fully differentiated by day 6 after induction.

METHOD DETAILS

Western blotting
Tissues were lysed by beat beating (TissueLyser II; Qiagen) or cells were scraped in adipocyte lysis buffer (ALB: 50 mM Tris, pH 7.4, 500 mM NaCl, 1% NP40, 20% glycerol, 2 mM EDTA supplemented with a cocktail of protease inhibitors (Roche)). Homogenates were centrifuged at 16,000 g x 10 min at 4°C, and the supernatants were used for subsequent analyses. Protein concentration was determined using the bicinchoninic acid assay (Pierce). Protein lysates were denatured in 4X NuPAGE LDS sample buffer (ThermoFischer; NP0007) containing 10% β-mercaptoethanol, resolved by 4%–12% NuPAGE Bis-Tris SDS–PAGE (Invitrogen) and transferred to a polyvinylidene difluoride (PVDF) membrane. Primary antibodies UCP1 (Abcam; AB10983), total OXPHOS (Abcam; AB110413), VCL (Sigma; V9264) and beta-actin (CST; 3700S)) were diluted in TBS containing 0.05% Tween (TBS-T), 5% BSA and 0.02% NaN$_3$ (Huttlin et al., 2010). Membranes were incubated overnight with primary antibodies at 4°C. For secondary antibody incubation, anti-rabbit or anti-mouse HRP (Promega) was diluted in TBS-T containing 5% milk. Results were visualized with enhanced chemiluminescence (ECL) western blotting substrates (Pierce).

Proteomics

Tissues were homogenized in 100 mM HEPES pH 8.5, 8 M urea, 2% SDS, 1p/15ml protease inhibitors (Thermo). The mixture was clarified by centrifugation and the supernatant was subjected to BCA protein concentration measurement, and reduced with 5 mM tris(2-carboxyethyl)phosphine (TCEP) and alkylated with 15 mM iodoacetamide. Proteins were then purified using the methanol-chloroform precipitation method and reconstituted in 200 mM EPPS at pH 8.5 and digested by Lys-C and trypsin overnight 1:100 enzyme-to-substrate ratio and an additional 6 h by trypsin the next day. Resulting peptides were labeled by TMT10plex or TMT-pro 16plex (Thermo) following the SL-TMT protocol (Navarrete-Perea et al., 2018), and quench by adding 5% hydroxylamine. A ratio-check is then performed by mixing 1% sample from each TMT channel, and the TMT-labeled peptides were evenly mixed based on the ratio-check. The mixture was desalted using Sep-pak cartridges (Waters), dried, and fractionated using an Agilent 1100 quaternary HPLC system. Peptides were separated using a 50 min linear gradient from 18% to 40% acetonitrile in 10 mM ammonium bicarbonate, pH 8, into a total of 96 fractions that were consolidated into 12 fractions. Samples were dried and desalted via StageTip and reconstituted in 5% formic acid and 5% ACN for liquid chromatography tandem mass spectrometry (LC–MS/MS) analysis.

Protein abundance was measured using an Orbitrap Fusion Lumos or Orbitrap Eclipse instrument. For measurements on the Orbitrap Fusion Lumos instrument, samples were analyzed using 180 min gradients at 500 nl/min flow rate. Fractionated peptides were injected. Tandem mass spectra (MS2) were matched in real time to targeted proteins (Schweppe et al., 2020). When a peptide match was observed to a targeted protein, a quantitative SPS-MS3 scan was acquired (McAlister et al., 2014). For protein abundance measurements on the Orbitrap Eclipse instrument coupled with an Easy-nLC 1200 (ThermoFisher Scientific) ultra-high-pressure liquid chromatography (HPLC) pump, all samples were analyzed with a 180 min gradient consisting of 2%–23% ACN, 0.125% FA at 500 nl/min flow rate. A FAIMSPro (Thermo) device for FAIMS separation of precursors (Schweppe et al., 2019). The FAIMS device was operated with default settings and multiple compensation voltages (40V/-60V/-80V). Under each FAIMS voltage, peptide ions were collected in data-dependent mode using a mass range of m/z 400 – 1600 using 2 sec cycles. Resolution for MS1 was set at 120,000, with standard automatic gain control (AGC) target. Multiply charged ions were selected and subjected to fragmentation at 35% normalized collisional energy (NCE) for MS2 with a dynamic exclusion of 120 s. Quantification was performed using multi-notch SPS-MS3 as described previously (McAlister et al., 2014).

The Comet algorithm (Eng et al., 2013) was used to search all MS/MS spectra against a database containing sequences of mouse (Mus Musculus) proteins downloaded from UniProt (http://www.uniprot.org). Reversed sequences were appended as decoys for FDR filtering, and common contaminant proteins (e.g. human keratins, trypsin) were included. Peptides were searched using following parameters: 25 ppm precursor mass tolerance; 1.0 Da product ion mass tolerance; fully tryptic digestion; up to three missed cleavages; variable modification: oxidation of methionine (+15.9949); static modifications: TMT 10plex (+229.162932) or TMT 16plex (+304.2071) on lysine and peptide N-terminus, carboxyamidomethylation (+57.0214637236) on cysteines. The target-decoy method was employed to control the false discovery rate (FDR)(Elias and Gygi, 2007; Huttlin et al., 2010; Peng et al., 2003). To distinguish correct and incorrect peptide identifications, linear discriminant analysis (LDA) was used to control peptide-level FDR to less than 1%. Peptides shorter than seven amino acids were discarded. Protein-level FDR was also controlled to 1% and as a result the number of peptide reverse hits were further decreased. Peptides were matched to the least number of proteins. TMT reporter ion signal-to-noise ratios for all quantified peptides matched to the same protein or site were summed up to report protein abundance. KEGG pathway GO enrichment analyses were performed using Enrichr, https://amp.pharm.mssm.edu/Enrichr/(Chen et al., 2013a; Kuleshov et al., 2016).

Determining % oxidation of cysteine residues in BAT

Tissue were homogenized in ice-cold 20% TCA using TissueLyser II (QIAGEN). Each lysate was split into two samples and washed with 20% TCA, 10% TCA, and 5% TCA twice. One half-sample was resuspended in blocking buffer (100 mM HEPES pH 8.5, 8 M urea, 2% SDS, 1 mM EDTA, 1 mM DTPA, 10 μM neocuproine, and 35 mM iodoacetamide) and incubating for 2 h at 37°C in the dark with shaking. The other half sample was treated with labeling buffer (100 mM HEPES, 8 M urea, 2% SDS, 1 mM EDTA, 1 mM DTPA, 10 μM neocuproine, and 35 mM cysteine phosophotag (CPT)). After samples were subject to methanol and chloroform precipitation. Protein pellets were resuspended in labeling buffer containing TCEP (5 mM) to label reversibly modified cysteines. Proteins were precipitated again and digested with LysC and trypsin as described above and reconstituted in 200 mM EPPS pH 8.0 and peptide concentration was determined by microBCA. Each half-sample (100 μg each) was TMT labeled as described above and a ratio-check was performed as described above. Samples were mixed according to ratios determined from the ratio-check. Combined samples were desalted using a Sep-Pak cartridge, treated with Lambda phosphatase, and enriched using IMAC. Enriched cysteine-containing peptides were then fractionated using a high pH reversed-phase peptide fractionation kit (Pierce), combined into six fractions, and purified by stage-tips. Peptides (1 μg/fraction) were run on a Orbitrap Eclipse as previously described (Mills et al., 2021). To calculate the % oxidation on cysteines TMT reporter ion signal-to-noise ratio (S/N) from the oxidized cysteine channel was divided by S/N from the fully TMT-labeled cysteine channel of the same protein to obtain the % reversible oxidation value.

Mitochondrial DNA damage

qPCR for murine mitochondrial (mt) DNA lesions was performed using following primers (10 μM): forward primer FWD: 5'-GCC AGC CTG ACC CAT AGC CAT AAT-3', reverse primer for the long 10090 bp PCR product: REV: 5'-GAG AGA TTT TAT GGG TGT AAT GCG G-3' and reverse primer for the short 127 bp PCR product: REV: 5'- GCC GGC TGC GTA TTC TAC GTT A -3'. qPCR was performed on

15 ng of sample DNA (extracted using the QIAGEN DNeasy blood and tissue kit) in 35 μl reactions on a PCR thermocycler (Biometra). 1 U TaKaRa LA Taq per reaction was used with its master mix. Linearity of the PCR reaction was confirmed for each sample by running a 1:2 diluted sample simultaneously. Cycling parameters for the short reaction were 94°C for 5 minutes followed by 16 cycles of 94°C for 30s, 64°C for 45s, 72°C for 45s, followed by 72°C for 10 minutes. Conditions for the long amplification were 94°C for 5 minutes, followed by 16 cycles of 94°C for 15s and 64°C for 12 minutes, followed by 72°C for 10 minutes. Concentrations of the PCR product were determined by measuring the emission of the samples at 488 nm and excitation at 525 nm after the addition of pico-green (Invitrogen) at 1:200 dilution. Amplification of the long product (>10 kb) normalized to amplification of the short template (100 bp) is used to assess the degree of mtDNA damage; more damage coincides with a decrease in amplification of the long template.

Measurement of mtDNA release

The release of mitochondrial and nuclear DNA into the circulation was assessed using the droplet digital polymerase chain reaction (ddPCR). Plasma samples were centrifuged (1600g for 10 min) and the supernatant was then centrifuged once more (16,000g for 10min) and DNA isolated using the DNeasy Blood kit (QIAGEN) according to the manufacturer's instructions, without step 3 (addition of lysis buffer AL). DNA was quantified using a 'Nanodrop' system and diluted to 1 ng/μL in elution buffer. For mtDNA the ND5 gene was assessed using the following primers: FWD- CTGCTCTTTCCCAGACGAGG; REV- AAGGCCACTTATCACCAGC. For nuclear DNA the β-actin gene was assessed, using FWD- ACCTAATTAAACACATCAACTTCCC; REV- GACTCAGTGCCAGGTTGTAA. Each PCR reaction (22 μL) comprised 1 μL (= 1 ng) DNA template, 11 μL ddPCR Supermix (no dUTP) containing Taq, 314nmol of each primer, and 210 nM of the FAM-β-actin probe (ATTGCCTTTCTGACTAGGTG) and of the HEX-ND5 probe (ACACCACCACATC AATCAAATTCTCCTTCA) probe and then made up to 22 μL with H_2O. The BIORAD ddPCR AutoDG was used to generate ddPCR droplets and the plate was sealed at 174°C before the PCR was run in a BIORAD C1000 Thermo Cycler using the following conditions: 95°C at 10 min followed by 40 cycles of 30 sec at 95°C and 1 min at 58°C and then 95°C at 10 min. After completion of the PCR, the fluorescence of the FAM and HEX probes was measured using the BIORAD QX200 Droplet Reader and analyzed using the BIORAD Quantilife software and Excel.

Determination of free-living whole-body total energy expenditure

Whole body energy expenditure in mice was determined using the energy balance method, otherwise known as the law of energy conservation, which accounts for caloric intake, change in body weight, and change in lean and fat mass throughout dietary intervention, as described previously (Goldgof et al., 2014; Guo and Hall, 2011; Ravussin et al., 2013). Briefly, individual mouse body weight and body composition were determined prior to dietary intervention. Throughout the twelve-week intervention period, mouse kcal intake was measured, as well as changes in body weight and body composition (fat mass and fat-free mass). Kcal intake was determined on the basis of the energy density of HFHS diet (5.5 kcal/gram), HFD (5.24 kcal/gram). Energy density of accumulated fat mass in mice was 9.4 kcal/gram and fat-free mass was 1.8 kcal/gram (Guo and Hall, 2011).

High-fat feeding

All mouse high-fat feeding experiments were performed with age-matched littermate controls. For high-fat high-sucrose intervention at eight weeks of age, mice were switched to high-fat high-sucrose diet (OpenSource Diets, D09071702) with 58% kcal% from fat, 28% kcal% from carbohydrate, and 15% kcal% from protein or high-fat diet (OpenSource Diets, D12492) with 60% kcal from fat, 20% kcal from carbohydrate, and 20% kcal from protein.

MitoQ supplementation

MitoQ was supplemented in drinking water at a concentration of 100 μM. MitoQ-containing drinking water was freshly prepared and replaced every three days.

β-estradiol treatment

0.25 mg 90-day release 17-β estradiol pellets (NE-121, Innovation research of America) were surgically implanted subcutaneously in 7-8-week old male WT and C253A C57BL/6 mice. Mice were analyzed 12 weeks post implantation.

13-Carbon glucose tracing

[U-^{13}C]-glucose (1 g/kg), (Cambridge Isotope Laboratories) was administered as a bolus over 20 seconds by tail vein injection for 15 mins prior to tissue harvest. Tissues were extracted and snap frozen in liquid nitrogen and stored at -80°C until MS analysis was performed.

Sample preparation for metabolite profiling

Sample preparation for metabolite profiling was performed as previously described (Xiao et al., 2020). Briefly, tissues were homogenized in 80% methanol containing inosine-^{15}N$_4$, thymine-d4 and glycocholate-d4 internal standards (Cambridge Isotope Laboratories; Andover, MA) at a 4:1 volume to wet weight ratio and centrifuged.

Metabolite analyses by mass spectrometry (LCMS)

All extracted samples were then subjected to LC/MS analysis as previously described (Xiao et al., 2020) using a Luna-amino column (Phenomenex) using an UltiMate-3000 TPLRS LC using a Q-ExactiveTM HF-X mass spectrometer (Thermo). Buffer composition was: mobile phase A (20 mM ammonium acetate and 20 mM ammonium hydroxide in 5:95 v/v acetonitrile/water) and mobile phase B (10 mM ammonium hydroxide in 75:25 v/v acetonitrile/methanol). A 10 min gradient from 10% to 99% mobile phase A was used to separate metabolites. Additional settings can be found as previously described (Xiao et al., 2020). Peak integrated was performed using TraceFinder software (Thermo Fisher Scientific).

Histological analysis and adipocyte size quantification

Tissues were fixed in 10% neutral buffer formalin overnight, embedded in paraffin, sectioned and mounted on glass slides and stained with hematoxylin and eosin. Images were collected with a Nikon Ti2 motorized inverted microscope and acquired with a Nikon DS-Fi1 color camera using NIS-Elements software. Analysis was performed using Fiji. For adipocyte size quantification microscopy images of BAT (20X magnification) and WAT (10X magnification) were digitally enhanced by the free Adipocount software (https://www.ncbi.nlm.nih.gov/pmc/articles/PMC5826178/) to increase the visibility of cell membranes. Faint membranes due to missing dye were detected and segmented by the software's algorithm. The resulting images were imported to ImageJ software containing the free Adiposoft plugin (https://imagej.net/plugins/adiposoft) for cell quantification. To measure size of adipocytes, the area parameter in Adiposoft was set to 0.323 μm/pixel and 0.645 μm/pixel for 20X and 10X images, respectively. Cells positioned at the edges of an image were excluded. The output data for each image contained the calculated area of all the adipocytes present in the image. Cells whose areas are smaller than 350 μm^2 were removed from the analysis as they could be a mixture of adipocytes and stromal vascular cells. The frequency of lipid droplet size was calculated using the Excel function (=frequency(data_array, bins_array)) with data_array = pooled data points and bins_array = distribution from 0 to 15,000 μm^2 in 500 increments. The frequencies were subsequently converted to percentages of total adipocytes counted. Finally, the Frequency (% total) vs. Adipocyte area (μm^2) plot was fitted into a Gaussian/Lorentzian distribution model using Prism.

Infrared image analysis

Infrared images of mice were taken using a FLIR thermal imaging camera (Model FLIR-T62101) as previously described (Okada et al., 2016). Briefly, images were taken with the FLIR camera and pictures were converted to Comma Separated Value (.CSV) files using the free FLIR Tools software (www.flir.com/products/flir-tools/). The.CSV files containing temperature data were then batch converted into.RAW image format using MATLAB script as previously reported (Okada et al., 2016) which can be imported into the free AMIDE medical imaging software (http://amide.sourceforge.net/) for temperature analysis. The.RAW files were imported to AMIDE and formatted as float, little endian (32-bit), 0 offset bytes, and 240 X 320 X 1 dimensions with voxel size of 1. Region of interest (ROI) boxes were drawn around the whole body, interscapular region, and tail. The ROI dimensions were adjusted for each image to ensure they were consistent in all mice. The mean temperature of the top 50% warmest area for each ROI was calculated in AMIDE and used for further analysis.

Body composition analysis

Body composition was examined with Echo MRI (Echo Medical Systems, Houston, Texas) using the 3-in-1 Echo MRI Composition Analyzer.

GTT

Mice were fasted for 6 h. Glucose (1 g/kg) was administered i.p., and blood glucose levels were measured at 0, 30, 60, 90 and 120 minutes using a glucometer.

Gene expression analysis

Total RNA was extracted from frozen tissue using TRIzol (Invitrogen), purified with a PureLink RNA Mini Kit (Invitrogen) and quantified using a Nanodrop 2000 UV-visible spectrophotometer. cDNA was prepared using 1 μg total RNA by a reverse transcription-polymerase chain reaction (RT-PCR) using a high-capacity cDNA reverse transcription kit (Applied Biosystems), according to the manufacturer's instructions. Real-time quantitative PCR (qPCR) was performed on cDNA using SYBR Green probes. qPCR was performed on a 7900 HT Fast Real-Time PCR System (Applied Biosystems) using GoTaq qPCR Master Mix (Promega). Reactions were performed in a 384-well format using an ABI PRISM 7900HT real time PCR system (Applied Biosystems). Fold changes in expression were calculated by the Delta Delta Ct method using mouse cyclophilin A as an endogenous control for mRNA expression. All fold changes are expressed normalized to the vehicle control. SYBR primer pair sequences can be found in Table S7.

Isolation of immune cells from fat and flow cytometry

Isolation of immune cells from BAT and subQ was performed as follows: fat pads were minced into small pieces with surgical scissors and transferred to a 15 ml falcon containing collagenase type II (Worthington; Cat# LS0041771; mg/ml; 7 ml) prepared in RPMI-1640 medium. Samples were digested for 30 mins at 37°C with shaking (200 rpm). After digestion samples were passed gently through 70 μm gauge mesh using a sterile syringe plunger and RPMI-1640 medium was added to 15 ml. Samples were centrifuged at 400 g for 5 min. Cells were resuspended in 400 μl FACs buffer (PBS containing 5% FCS). Single-cell suspensions were incubated

with Fc-receptor-blocking antibody (14-0161-82; eBioscience) before being stained at 4 degrees. Dead cells were excluded with a live/dead Zombie Aqua stain (BioLegend). Antibodies were as follows: CD19 (6D5), CD3 (17A2), CD8a (53-6.7), CD4 (GK1.5), CD11c (N418), CD45 (30-F11), and F4/80 (BM8) were purchased from BioLengend, and CD11b (M1/70) was purchased from eBioscience. Samples were fixed using a fixation buffer (BioLegend) and absolute cell counts were determined using count beads (Spherotech; ACFD-50-5). After being stained, cells were passed through a 70 μm filter and analyzed on a LSRFortessa (BD Biosciences) with FACSDiva software. Analysis of the stained populations was performed by gating on single, live cells. Gating strategy is illustrated in supplemental information. Flow cytometry data were analyzed with FlowJo v10 software (Tree Star).

Cellular respirometry of primary brown adipocytes

Cellular OCR of primary brown adipocytes was determined using a Seahorse XF24 Extracellular Flux Analyzer. Adipocytes were plated and differentiated in XF24 V7 cell culture microplates. Prior to analysis adipocyte culture medium was changed to respiration medium consisting of DMEM lacking NaHCO$_3$ (Sigma), NaCl (1.85 g/L), phenol red (3 mg/L), 2% fatty acid free BSA, and sodium pyruvate (1 mM), pH 7.4. Basal respiration was determined to be the OCR in the presence of substrate (1 mM sodium pyruvate) alone. Respiration uncoupled from ATP synthesis was determined following addition of oligomycin (4.16 μM). Maximal respiration was determined following addition of DNP (2 mM). Rotenone (3 μM) and antimycin (3 μM) were used to abolish mitochondrial respiration. Leak respiration was calculated as OCR following rotenone/antimycin treatment subtracted from OCR following oligomycin treatment.

Indirect calorimetry

Energy expenditure, VO$_2$, VCO$_2$, food intake and movement were assessed using the Sable Systems' Promethion apparatus which consisted of a rack of 16 metabolic cages and another of 8 metabolic cages. Mice were fed *ad libitum* with standard rodent chow for the duration of the experiment. This apparatus was enclosed in a temperature-controlled chamber and over the course of the experiment the temperature was adjusted as depicted in the graphs ranging from 4°C to 29°C. Mice were injected i.p. with CL-316,243 (1 mg/kg) as depicted. Macro 13, from the Expedata software system, was used to export metabolic variables of interest at each reading for each cage.

Statistical analyses

Data were expressed as mean ± s.e.m. and P values were calculated using two-tailed Student's t-test for pairwise comparison of variables, one-way ANOVA for multiple comparison of variables, two-way ANOVA for multiple comparisons involving two independent variables, and ANCOVA for energy expenditure analyses. ANOVA analyses were subjected to Bonferroni's post hoc test. Sample sizes were determined on the basis of previous experiments using similar methodologies. For all experiments, all stated replicates are biological replicates. For *in vivo* studies, mice were randomly assigned to treatment groups. For MS analyses, samples were processed in random order and experimenters were blinded to experimental conditions.